Department of Geological Sciences
Jadavpur University
Kolkata 700032
India

Dr. Tridib Kumar Mondal
Assistant Professor
Tel: (Office) +91 033 2457 2553
Fax: +91 033 2457 2719
e-mail: tridibkumarmondal@gmail.com

7th May 2020

To
Prof. Soliva Roger
The guest editor
Special Issue in Solid Earth

Subject: Submission of the REVISED MANUSCRIPT for the Special Issue in Solid Earth entitled "Faults, fractures, and fluid flow in the shallow crust".

Dear Editor,
Thank you for your helpful comments on the manuscript se-2020-30. We have addressed all the issues raised by you in our replies below and in most cases have modified the manuscript accordingly.

Editor's comment: *1 - Please remove the new text about KIC, which is inappropriate to the study case. First this rationale implies too much speculation about the initial crack length, which is not observed or at least not presented. Second, you try to estimate the stress with a LEFM equation in which you have two unknowns (Y and S3). Third, you give phenocryst size to define a potential length of initial crack (which is very speculative) to use this equation which is for homogeneous elastic properties. In you rationale, the crack length is controlled by the penocrist and host heterogeneity and therfore not controlled by the elastic stresses. Then the rational is not suitable.*

Authors' response: Accepted and deleted from the manuscript.

Editor's comment: *You can let the following text and mention briefly how S3 has been estimated if the estimation is proper (LOT ?): « It may also be noted that, previous studies by Mondal and Acharyya, 2018, conducted in Chitradurga Granite, in close vicinity of the study area also regarded the magnitude of σ3 ~10 MPa, to be a good estimation. Combining these estimations with the results obtained from the present studies, we constrained the value for σ3 ~12MPa. »*

Authors' response: Accepted (The estimation was based on the fracture toughness values).

Editor's comment: *2 - Please clearly answer to the following reviewer#2 main comment that you have not considered in your revision:*
Reviewer #2 mentionned : « In page 14 (lines 273-274), it is mentioned: "Tensile strength of metabasalt (~12MPa; obtained from BTS studies) indicates that the minimum principal stress (sigma3)has to be sigma3≥12 MPa." Thereafter, this value is selected as magnitude for theminimum principal stress for the stress reconstructions (e.g. Fig. 7). I am particularly puzzled by the reasoning. The condition for tensile fracturing is sigma3 – pore pressureless or equal to the negative value of tensile strength. That is if sigma3 = 12 MPa thenPf has to be equal or higher than 24 MPa... Starting from there could the authorsexplain how they constrain sigma3? »
I completely agree with reviewer 2, there is again a problem of rationale, or unclear/incomplete explanation. First, I do not understand how you use the BTS to estimate the minimum principal stress. The BTS gives you an estimate of the strength (a negative stress value) but this value alone can not give you the full minimum principal stress (Sigma 3, which must be positive at depth). Then BTS gives you T0

= -12 MPa. If you manage to estimate S3 (how ?) as equal to 12 MPa (then positive), then Pf must be higher or equal to S3+(-T0), then 24 MPa as suggested by the reviewer.

Authors' response: We are extremely grateful to you for pointing out this sections that we failed to communicate in a better way. We feel there has been some drawbacks from our side that we failed to explain our viewpoint. In the following we have tried to clarify your concerns regarding the manuscript. The equation that we could not justify $\sigma_3 - P_f \geq T$ (after Gudmundsson, 2011) explains the formation of hydro-fractures at any depth. In our study, we have shown the role of pre-existing anisotropy and fractures/faults in channelizing fluid flow. Fluid plays a vital role in reactivating the pre-existing fractures, but the formation of fractures is driven by the tectonic stresses. The P_f is negligible when the fracture system consisting of the riedel shear components, P, Y, R, T, X and R´ shears are formed due to the sinistral movement along CSZ, that acted as the shear boundary under a WNW-ESE directed D3 compression. Therefore, the condition that we presumed, satisfies the equation $\sigma_3 \geq T$ (You, 2015). The studies by Ishii (2015) have shown that the laboratory-measured tensile strength is almost similar to the tensile crack initiation stress (σ_3). Eidelman and Reches (1992) have also shown that the minimum principal stress required for the generation of fractures in stiff inclusions (such as pebbles) may be considered to be identical to the laboratory measured tensile strength of the rock. Therefore, we have considered that the minimum principal stress (σ_3) required for fracture initiation in the metabasalt of the study area are equivalent to its tensile strength. In the present study, we used BTS to quantify the tensile strength of the metabasalts (T=12 MPa). It may be noted that, for quantifying σ_3, we only considered the magnitude of the tensile strength here. We agree that the magnitude of σ_3 could be greater than the one we considered, but as we are dealing with the limiting condition this is the minimum magnitude of σ_3 required to overcome the tensile strength of the rock and generate a fracture in the rocks. In the revised manuscript the changes are marked in blue color in line number 296-305.

Editor's comment: *3 - You mention « CORRECTED and INCORPORATED the suggestion » for the following comment I mentionned: « Provide more justification in the discussion about the deformation mechanism related to the magnetic fabric. Can we interpret the magnetic fabric as non-coaxial (simple shear) or multi episodic deformation (2 poles on the stereogram), and then having a shortening oblique to the foliation ? »*
Please, clearly indicate in which lines you did the explanation, I do not find dit in the Ms.

Authors' response: We would like to thank you for raising this issue and giving us an opportunity to revise the same. Yes, we extremely apologize for this inadvertent error. We had added some words that somehow got deleted while editing.

The NNW-SSE to NW-SE oriented magnetic fabric has developed during regional D1/D2 deformation on account of ~NE-SW directed shortening and that is characterized as a co-axial deformation. Recent studies by Mondal (2018) also suggest that, the same ~NW-SE oriented magnetic fabric in the adjacent Chitradurga granite is a product of co-axial deformation (D1/D2) manifested by NE-SW shortening. Since the magnetic fabric has a range of strike orientation (NW-SE to NNW-SSE), thus producing a variation (spreading) of its pole in the lower hemisphere equal area projection.
The line number 384-391 in section 5.1 of the revised manuscript reads as follows: "This implies that the fabric in metabasalts of the study area must have been controlled by the regional D1/D2 deformation under ~NE-SW directed shortening that generated the field foliation in the meta-sedimentary sequences. Recently Mondal and Mamtani (2014) and Mondal (2018) interpreted that, the ~NW-SE oriented magnetic fabric in the adjacent younger granites of the study area are the result of co-axial (pure shear) deformation. Since these fabric in metabasalts and adjacent younger granites are found to be parallel and manifested by the same NE-SW shortening, it is inferred that magnetic fabric in the metabasalts of the study area are also the result of co-axial deformation."

Editor's comment: *4 - The wing crack geometry has not been corrected in the block diagrams of the last figure although you mention that you did the revision. The wing crack geometry you drawn is still kinematically inconsistent with the sense of shear on the reactivated veins in the three schemes and at different places in a same sheme. The wing cracks you drawn around the reactivated veins suggest right lateral shear, which is inconsistent with the far field stress. Please revise the wing crack position in all the diagrams to adapt them to sinistral shear on the slipped veins, and to be consistent with the remote stresses.*

Authors' response: You have also raised your concern regarding the wing cracks in Fig. 11 of the revised manuscript. However, we would like to mention here that all the cracks that you have mentioned are not wing cracks. Moreover, these are the various components of riedel shear system that are reactivated during vein emplacement. In accordance with your recommendations again we have modified the same (see below) for the clarity of the manuscript.

With the above revisions we hope that all the questions have been addressed and the revised version of manuscript is to your satisfaction.
Thanking you
Yours sincerely
Tridib Kumar Mondal
(Corresponding author)

Figure: 11

Control of pre-existing fabric in fracture formation, reactivation and vein emplacement under variable fluid pressure conditions: An example from Archean Greenstone belt, India.

Sreyashi Bhowmick and Tridib Kumar Mondal

Department of Geological Sciences, Jadavpur University

5   Kolkata-700032, West Bengal, India

*Corresponding author: **Tridib Kumar Mondal (tridibkumarmondal@gmail.com)**

Alternate E-mail: **tridibk.mondal@jadavpuruniversity.in**

Abstract

10   Most of the upper crustal fluid flows are strongly influenced by the pre-existing fractures/foliations in the rocks under a certain state of tectonic stress and fluid pressure condition. In the present study, we analysed a wide range of crosscutting fractures that are filled with quartz veins of variable orientations and thicknesses, from the gold bearing massive metabasalts (supracrustal) of the Chitradurga Schist Belt adjacent to the Chitradurga Shear Zone (CSZ), western Dharwar craton, south India. The study involves

15   the following steps: 1) analysing the internal magnetic fabric using anisotropy of magnetic susceptibility (AMS) studies, and strength of the host metabasalts, 2) quantifying the fluid pressure condition through lower hemisphere equal area projection of pole to veins by determining the driving pressure ratio (R′), stress ratio (ϕ), and susceptibility to fracturing, and 3) deciphering the paleostress condition using fault slip analysis. We interpret that the NNW-SSE to NW-SE (mean 337 º/69º NE) oriented magnetic fabric

20   in the rocks of the region developed during regional D1/D2 deformation on account of NE-SW shortening. However, D3 deformation manifested by NW-SE to E-W shortening led to the sinistral movement along

CSZ. As a consequence of this sinistral shearing, fractures with prominent orientations formed riedel shear components, with CSZ as the shear boundary. Subsequently, all the pre-existing fabrics along with the riedel shear components were reactivated and vein emplacement took place through episodic fluid pressure fluctuation from high to low P_f at shallow depth (~2.4 Km). However, NNW-SSE orientations were susceptible to reactivate under both high and low P_f conditions thereby attaining maximum vein thickness along these orientations. The deduced paleostress from fault-slip analysis, along with the kinematics of the fractures and veins are in good agreement with previously estimated regional tectonics. Thus, integrating multiple domains of studies, help in the logical interpretation of fluid flow condition and vein emplacement mechanism in the study area that has not been ventured before.

1. Introduction

The upper crust is replete with fractures/faults, which act as pathways for fluid flow and vein emplacement. Fracture formation and vein emplacement mechanisms are closely interrelated, and require a detailed study for finding out potential hydrothermal deposits. Fracture formation and reactivation involves a combination of regional stress field (far field stress), stress ratio (Φ) and driving pressure ratio (R´) that helps to determine the prevailing fluid pressure condition (Delaney et al., 1986; Jolly and Sanderson, 1997; McKeagney et al., 2004; Mazzarini and Isola, 2007; Martinez-Poza et al., 2016; Cucci et al., 2017). However, previous studies suggest that pre-existing anisotropy in host rocks play a significant role in formation and propagation of fractures provided the anisotropy is favorably oriented to the far field stresses (Ikari et al., 2015; Donath, 1961; Hoek, 1964; Attwell and Sandford, 1974). Presence

of such favorably oriented anisotropy lowers the shear strength of the host rocks, enabling failure/slip along them at minimum compressive stress, prior to/during vein emplacement. Such conduits are reactivated at both high and low fluid pressures forming pathways for fluid flow (Mondal and Mamtani 2013, Lahiri and Mamtani, 2016). Thus, vein emplacement mechanism requires favorably oriented fractures that can be reactivated, when fluid pressure gradually builds and exceeds the normal stresses acting on the fracture wall (Gudmundsson, 2011). This enables the fractures to open up, under cyclic increase of fluid pressure along such pre-existing conduits, a mechanism known as *fault-valve action* (Sibson et al., 1988; Sibson, 1992, 1996, 2000; Boullier and Robert, 1992; Sibson and Scott, 1998; Petit et al., 1999; Cox et al., 2001 among others). Subsequently, fluid flows into the fractures, a phenomenon analogous to *burping*, triggering an immediate drop in fluid pressure. This sudden drop in fluid pressure is responsible for mineral deposition and vein formation (Cox et al., 1991, Cox, 1995; 2001). Vein materials thus deposited seals the fracture/fault planes, preparing the system for the next cycle of fluid pressure build up, rupture, fluid flow and vein formation (Mondal and Mamtani, 2013; Lahiri and Mamtani, 2016; Marchesini et al., 2019). Thus, repeated cycles of elevated and depleted fluid pressure generate widespread networking of veins in host rocks. Studies conducted in this approach help to understand the mechanism of fabric development and fracture formation vis-à-vis vein emplacement. This study also aims to provide a detailed insight about the development of brittle structures and their role in understanding the tectonic evolution of Archean cratons.

The Chitradurga Schist belt (western Dharwar craton, south India), is a NW-SE trending Archean greenstone belt, known to harbor a widespread network of veins with potential epigenetic gold bearing lodes (Gupta et al., 2014; Gopalakrishna et al., 2018). We have conducted this study in the meta-volcanic

(metabasalt), hosting quartz veins of variable orientations and thicknesses, in and around Chitradurga region. We emphasize on understanding the mechanism of vein emplacement under a tectonic environment where propensity of fracture reactivation for vein emplacement is mutually dependent on both fluid pressure condition and the regional far field stresses. The present paper is a comprehensive work which quantifies the fabric in the visually isotropic metabasalts of the Chitradurga Greenstone belt and its role in fracture formation and in channelizing upper crustal fluids. We also found the potential reactivation ability of the fractures/faults at variable fluid pressure conditions to investigate the role of fractures/faults which are not favorably oriented to the pre-existing anisotropy and regional stress field, and their contribution for vein emplacement in the study area.

2. Geology of the study area

The study has been conducted in the Chitradurga Greenstone Belt of Dharwar craton (southern India; Fig. 1a), which represents a complex geological history. Dharwar craton exposes >3.0 Ga, Archean continental crusts, represented by the TTG (trondjemite-tonalite-granodiorite gneiss) also known as the peninsular gneiss (Jayananda et al., 2006). The craton stabilized during the accretion of Eastern Dharwar Craton (EDC) and Western Dharwar Craton (WDC) at 2.75-2.51 Ga. The zone of accretion of the two tectonic blocks is marked by a shear zone, referred to as Chitradurga Shear Zone (e.g., Naqvi and Rogers, 1987; Chadwick et al., 2003; Jayananda et al. 2006). The eastern part of WDC marked by Chitradurga Schist Belt (CSB) (Fig. 1b), comprises of peninsular gneiss (3.4-3.0 Ga), and younger supracrustal rocks (Beckinsale et al., 1980; Sarma et al., 2011; Taylor et al., 1984). The latter comprises metavolcanics/metabasalts (greenstone belt; greenschist/lower amphibolite facies metamorphism),

metamorphosed greywacke-argillite (interbanded with ferruginous chert and banded iron formation), polymict conglomerate, and ferruginous chert. The basaltic rocks of the schist belt have an island arc affinity (Chakrabarti et al., 2006). Regionally, the belt is surrounded by older peninsular gneisses and younger granitoids (Ramakrishna and Vaidyanadhan, 2010). Previous geological investigations, revealed the presence of various younger granites ~2.6 Ga; (Jayananda et al., 2006; Chardon et al., 2002) which are associated with the schist belt, such as Chitradurga granite, J. N. Kote granite. The structural investigations of the adjacent meta-sedimentary rocks of the region show that the area has undergone three phases of deformation: D1, D2 and D3 respectively (Chadwick et al., 1989; Jayananda et al., 2006; Mondal and Mamtani, 2014).The D1/D2 deformations are coaxial with NW-SE striking axial plane. D1 folds are tight to isoclinal and asymmetric while the D2 folds are open to tight and upright. Earlier studies revealed that the folds (regional open; NE-SW striking vertical axial plane), related to early D3 deformation superposed the D1/D2 structures thus resulting in dome-basin geometry in the meta-sedimentary rocks of that region (Chakrabarti et al., 2006; Mondal and Mamtani, 2014). However, later phase of D3 deformation led to the formation of brittle structures in the younger granites of CSB (Mondal and Mamtani, 2016). The NE-SW shortening during D1/D2 deformation was responsible for NW-SE oriented structural elements in the CSB (Chadwick et al., 2003), while NW-SE to E-W shortening direction prevailed during D3 deformation (Jayananda et al., 2006; Mondal, 2018; Mondal and Acharyya, 2018). A number of petrological and geochemical investigations have been carried out on the area in the past. These studies suggest the presence of actinolite, albite, chlorite, epidote, quartz and calcite in the basaltic rocks (Chakrabarti et al., 2006). The CSB holds evidence of progressive metamorphism with a gradual increase in P-T conditions (approximately 3-4 Kb of pressure), from greenschist facies in the

north to amphibolite facies in the south suggesting the depth of deformation to be 10-12 Km (during D1/D2). However, recent studies by Acharyya and Mondal, (2019) shows that the brittle deformation during late D3 took place at a shallow depth of ~2-4 km. The dashed rectangular area in figure 1b demarcates the study area. The present study focuses on the dark greyish to blackish, massive to fine grained, altered metabasalt hosting quartz veins, of the region surrounded by meta-sedimentary sequences (Fig. 2). The metabasalts of the study area are devoid of any well-defined mesoscopic foliation. The foliation planes in the adjacent meta-sedimentary rocks of the region are found to be NW-SE oriented (mean strike/dip is 323º/71º NE). Since, the metabasalts are devoid of mesoscopic field fabric, the anisotropy of magnetic susceptibility (AMS) study has been conducted in order to quantify their internal magnetic fabric.

3. Overview of brittle structures

Metabasalts of the study area are replete with fractures and faults of multiple orientations. Some of these fractures and faults are found to host quartz veins forming criss-cross pattern (Fig. 3a and c) and some of them are devoid of any vein material. Growth of vein materials (quartz crystals) are often found to be perpendicular to the vein wall suggesting that dilation was significant in these veins (Fig.3b). The maximum width and length of the quartz veins are ~1 meter and ~130 meters respectively. Some of the quartz veins are found to be displaced by other ones forming crisscross network of veins in the study area (Fig. 3c). Wing cracks filled up with quartz veins are also observed (Fig. 3d). At few places, the thicker quartz veins show series of successive fault planes with slickenside lineations on them (Fig. 3e and *in-set*). Those veins are often found to enclose angular metabasalt enclaves (host material, Fig. 3f),

suggesting that fault valve action was predominant in the region. Quartz veins are recorded with multiple median lines as an evidence of crack-seal mechanism due to cyclic fluid ingression (Fig. 3g). Some of the fault planes recorded in the study area have shallow plunging slickenside lineations while others have moderate to high plunge. Both Left Lateral Faults (LLF's) and Right Lateral Faults (RLF's) are recorded based on the movement of the hanging wall with respect to the footwall. Presence of congruous steps helps in the discrete identification of the fault planes (Fig. 3h). Although, quartz veins of variable orientations and thicknesses are found, however, most of the veins are predominantly NNW-SSE trending (Fig. 4a). Most of the fractures and faults show NNW-SSE trend (maxima) whereas some others form a WNW-ESE to NE-SW sub maxima respectively (Fig. 4b & 4c). Some WNW-ESE trending Mode-I (tensional) cracks with prominent tips are also recorded from the study area which are often filled up with quartz veins. It may be noted that the veins with maximum thicknesses are oriented along NNW-SSE direction (Fig. 4d). In this study, 992 fracture data (strike/dip), 378 vein data (strike, dip and thickness) and 73 fault data (strike, dip and slip) have been measured from the metabasalt exposures at about 13 locations in the entire study area. All 73 shallow to moderately plunging fault planes are used to decipher the paleostress condition. Thus, the strict spatial and temporal relationships between brittle structures and veins provided by field observations help to quantify the fluid pressure conditions that prevailed during fracture reactivation and vein emplacement. It also provides information for reconstructing the tectonic stress conditions of the craton.

4. Methods of analysis and results

The quartz veins have been emplaced in the massive metabasalts of the region that are devoid of any prominent mesoscopic foliation as mentioned above. At places, veins of one orientation are dissected and sometimes displaced by others that led to the formation of mesh like structures (Fig. 3a, c). Sibson (1992) has mentioned that such a mesh is formed when a rock contains fractures of variable orientations that may get reactivated due to rise in fluid pressure. It is mentioned that in the Chitradurga region, veins of various orientations show mutually cross-cutting relationships, which implies repeated cycles of vein emplacement (see section 3; Mondal and Mamtani, 2013; Sibson, 1992). Although veins have various orientations, NNW-SSE striking veins are the most common (Fig. 4a). It may be noted that NW-SE to NNW-SSE direction, which defines the maximum strike orientation of quartz veins, fractures and faults, is also the orientation of the adjacent Chitradurga shear zone, the overall trend of the schist belt. This implies that there is a strong structural control on the formation of these quartz veins. It has been shown earlier that the pre-existing anisotropy plays a critical role in propagating fractures and channelizing fluid in rocks (Sanderson and Zhang, 1999, Cox et al., 2001 and Ikari et al., 2015). It is also known from rock mechanics investigations that the rock strength variation controls the strain partitioning and influences fluid flow (e.g., Tsidzi, 1990; Vishnu et al 2018). Therefore, it is crucial to determine the orientation of anisotropy in host rocks and the state of stresses governing the upper crustal fluid flow vis-à-vis vein emplacement.

3-D Mohr circle analysis has been performed by Jolly and Sanderson (1997) using dyke orientation data to examine the magma pressure condition that was responsible for the opening of pre-existing fractures during dyke emplacement. Further the work has been extended to understand the fluid pressure condition and vein emplacement mechanism by McKeagney et al., 2004 (also see Yamaji et al., 2010).We present

vein orientation data from the Chitradurga region (southern India), which is a province of epigenetic gold deposit (Gupta et al., 2014;Gopalakrishna et al., 2018).

We conduct anisotropy of magnetic susceptibility (AMS) study, followed by Brazilian Tensile strength (BTS) determination in order to quantify the internal magnetic fabric and tensile strength of the rocks within the study area. The 3-D Mohr circle construction using quartz vein orientation data helps to recognise the fluid pressure conditions under which they were emplaced. Further, these fluid pressure conditions were integrated with dilation tendency, slip tendency and fracture susceptibility in order to understand the mechanism of vein emplacement in the Chitradurga region. A combination of data obtained from these methods along with paleostress analysis using fault-slip data recorded from the study area provides a comprehensive evaluation of vein forming conditions in Chitradurga greenstone belt.

4.1 Anisotropy of Magnetic Susceptibility (AMS)

The quartz veins occur in massive metabasalt, which does not show any visible field foliation. However, such visibly massive rocks may preserve an internal fabric, which can be recognized through anisotropy of magnetic susceptibility (AMS) studies (e.g., Tarling and Hrouda, 1993; Maffione et al., 2015; Mamtani and Greiling, 2005; Raposo et al., 2007; Loock et al., 2008; Mondal and Mamtani, 2014; Mondal, 2018). The study involves preparation of cylindrical core samples (25.4 mm diameter × 22 mm height) from oriented metabasalt blocks. These metabasalt block samples have been collected from 13 different locations (Fig. 5) in the study area. The prepared core samples are subjected to an external magnetic field and the induced magnetization for each core sample is measured in different directions. AMS is considered to be a symmetric second-rank tensor, represented by an ellipsoid with three mutually

perpendicular principal axes, K_1, K_2 and K_3 respectively where ($K_1 \geq K_2 \geq K_3$). The orientation and magnitude of each of these principal axes are determined in this analysis, where K_1 represents the magnetic lineation, K_3 is the pole to the magnetic foliation (K_1K_2). Using the magnitudes of K_1, K_2 and K_3, several AMS parameters are calculated such as magnetic susceptibility (K_m), magnitude of the magnetic foliation (F) and magnetic lineation (L), degree of magnetic anisotropy (P_j or P') and shape parameter (T). The formulae for the parameters are given below (after Tarling and Hrouda, 1993; Jelínek, 1981):

$$K_m = (K_1+K_2+K_3) / 3, \tag{1}$$

$$F = (K_2-K_3) / K_m, \tag{2}$$

$$L = (K_1-K_2) / K_m, \tag{3}$$

$$P_j = \exp \sqrt{\{2\,[(\eta_1-\eta_m)^2 + (\eta_2-\eta_m)^2 + (\eta_3-\eta_m)^2]\}}, \tag{4}$$

$$T = (2\eta_2-\eta_1-\eta_3) / (\eta_1-\eta_3), \tag{5}$$

Here, $\eta_1 = \ln K_1$, $\eta_2 = \ln K_2$, $\eta_3 = \ln K_3$ and $\eta_m = (\eta_1.\eta_2.\eta_3)^{1/3}$. In the above equations, P_j and T give the measure of the eccentricity and shape of the AMS ellipsoid respectively. The value of T ranges between -1 to +1. Positive and negative values represent oblate and prolate shapes of the AMS ellipsoid (Tarling and Hrouda, 1993).

AMS measurements have been conducted in the spinner mode (field intensity of 300 Am^{-1}) using the KLY-4S Kappabridge (AGICO, Czech Republic); see Hrouda et al. (2006) for instrument details. The SUFAR program has been used to calculate the required AMS parameters described above for each sample. A total of 65 cores are prepared and analysed. The mean value of the AMS parameters at each

location is calculated using the program Anisoft (version 4.2, AGICO; Jelinek statistics, Jelinek, 1981).It

is noted that the K_m varies between 37 and 1280 $\times$ 10^{-6} SI units, with most of the samples having K_m below

210   1000 $\times$ 10^{-6} SI units (see supplementary sheet-1). This indicates that paramagnetic and ferromagnetic

minerals contribute significantly to the AMS. Petrographic studies reveal the presence of actinolite,

hornblende, chlorite, albite, epidote, pyrite which are inferred to contribute to the susceptibilities recorded

in the samples. The P_j lies between 1.003 and 1.539, and the shape of the AMS ellipsoid is dominantly

oblate (positive T values; see supplementary sheet-1). It is noted that the magnetic foliation (K_1K_2 plane)

215   is consistently NW-SE striking (mean orientation: 337º/69º towards NE; Fig. 5a). The magnetic lineations

plunge variably from NNW, through sub-vertical to SSE (Fig. 5b).

4.2 Tensile strength determination

It is known that the dilation occurs in a direction parallel to the minimum compressive principal

220   stress (σ_3), when the fluid pressure (P_f) exceeds the normal stress acting on the fracture wall.

Therefore, the fractures may occur at any depth when the effective stress ($\sigma_3 - P_f$) is sufficient to

counteract the tensile strength (T) of the rocks (Gudmundsson, 2011). We measure the tensile

strength of the host metabasalts to quantify the P_f that prevailed during vein emplacement in the

region. The measurement of direct tensile strength requires machined specimens and also involves

225   difficulty in applying tensile load on the cylindrical specimen during analysis. Therefore, tensile

strength measurement of rocks using Brazilian test has become imperative in rock mechanics.

Compression-induced extensional fractures are generated in the test which essentially involves line-

loading on a circular disk placed between two platens (Aydin and Basu, 2006; Basu et al., 2013; see

Fig.6).This tensile strength (T) is estimated from the elastic theory (ISRM, 1978; ASTM D3967, 2001):

$$T = \frac{2P}{\pi LD} \; .$$

(6)

Here, P is peak/failure load, and L and D, are the length and diameter of the disk respectively. For this analysis, 18 core samples were drilled from metabasalt blocks which were later resized to obtain the desirable cores for the analysis (length: diameter = 1: 2). The maximum tensile strength of each specimen at the instance of failure is recorded. The maximum tensile strength for 18 samples is averaged out to obtain the approximate tensile strength of metabasalts, which is ~12 MPa. This tensile strength value is further used for quantifying the P_f in 3D Mohr circle using vein orientation data.

4.3 Fluid pressure determination

Here, we have used the method proposed by Jolly and Sanderson (1997) to quantify the P_f conditions that led to the vein emplacement in metabasalts of Chitradurga region (southern India). We have used the lower hemisphere equal area projection of the poles to quartz vein data. According to Jolly and Sanderson (1997), girdle distribution of vein pole data implies $P_f > \sigma_2$, described as a condition where large number of fracture orientations are susceptible to reactivate, while $P_f < \sigma_2$, represents clustered distribution of vein pole data, where only limited range of fracture orientations reactivate. Depending on the type of distribution (girdle/cluster), parameters such as stress ratio (ϕ) and driving pressure ratio (R′) are

calculated using ranges of fracture orientations (θ_1, θ_2 and θ_3) from the following equations provided by Jolly and Sanderson, 1997 and Baer et al., 1994.

$$R' = \frac{P_f - \sigma_3}{\sigma_1 - \sigma_3} = \frac{1 + cos2\theta_2}{2}. \tag{7}$$

250 For $P_f > \sigma_2$,

$$\Phi = \frac{\sigma_2 - \sigma_3}{\sigma_1 - \sigma_3} = 1 - \frac{1 - cos2\theta_2}{1 - cos2\theta_3}. \tag{8}$$

For $P_f < \sigma_2$,

$$\Phi = \frac{\sigma_2 - \sigma_3}{\sigma_1 - \sigma_3} = \frac{1 + cos2\theta_2}{1 + cos2\theta_1}. \tag{9}$$

In figure 7a, the lower hemisphere equal area projection of pole to vein data shows girdle distribution,

255 implying high fluid pressure condition ($P_f > \sigma_2$). From this distribution the orientations of the principal stress axes (σ_1, σ_2 and σ_3) are determined using the Bingham statistics of the Stereonet 9 software (**http://www.geo.cornell.edu/geology/faculty/RWA/programs/stereonet.html**). σ_1 is sub-vertical lying in the empty space devoid of any vein pole data. Subsequently, following Jolly and Sanderson (1997), the planes $\sigma_1\sigma_2$, $\sigma_1\sigma_3$ and $\sigma_2\sigma_3$ are constructed and the range of fracture orientations, θ_2 and θ_3 are determined

260 along the $\sigma_1\sigma_3$ and $\sigma_1\sigma_2$ planes respectively. For this high P_f condition, $\theta_2 = 27^\circ$, $\theta_3 = 59^\circ$ from which $\phi = 0.72$ and $R' = 0.8$ are calculated. Thus, such a P_f condition enhances the chances of vein emplacement along various orientations. Although pole to vein data represents a girdle distribution pattern, however the distribution of the data points shows three prominent clusters. The WSW cluster forms the highest density cluster around the σ_3 axis indicating a number of veins with similar orientations. The cluster

265 primarily represents the NNW-SSE to NW-SE trending veins, attaining the maximum thickness. It is to

be noted that majority of the veins are oriented along this direction (see Fig. 4a), which also suggests that the vein forming fluid must have been channelized through a pre-existing anisotropy (trending NW-SE to NNW-SSE, see section *4.1*). These data are segregated and plotted separately in the lower hemisphere equal area projection and thus the obtained contour defines the WSW cluster (Fig. 7c). We decided to extend the contour interval beyond the data points in order to incorporate the maximum range of vein orientations (θ) lying parallel/sub-parallel to the internal anisotropy (as evident from the anisotropy of magnetic susceptibility study) of the host rock. Also, the contour interval and significance level for each of the clusters were selected in such a way that maximum number of data points are included, in order to obtain a statistically viable data cluster. Apart from the WSW cluster (with a high cluster density), the SE and the NE clusters (with higher data spreading) are also evaluated discretely (Fig. 8). The number of obtained clusters can also be testified through mixed Bingham analysis using **K** vs BIC (i.e., the number of Bingham component of a mixed Bingham distribution vs Bayesian information criterion; Yamaji and Sato, 2011). We have found that the lowest BIC values are obtained when **K**=3 (number of possible clusters for the given data set), thereby, justifying the selection of the three clusters for the analysis. It is however difficult to quantify the lowest P_f value; we therefore intend to use the obtained P_f values from the respective clusters as examples of low P_f conditions denoting P_f fluctuation rather than quantifying the lowest P_f condition of the study area. The orientations of the principal stress axes (σ_1, σ_2 and σ_3) are determined using the Bingham statistics of the Stereonet 9 software. Similarly, the $\sigma_1\sigma_2$, $\sigma_1\sigma_3$ and $\sigma_2\sigma_3$ planes are constructed and the range of fracture orientations θ_1 and θ_2, are calculated along the $\sigma_2\sigma_3$ and $\sigma_1\sigma_3$ planes. Again, for low P_f conditions, $\theta_1 = 38°$, $\theta_2 = 43.2°$, $\phi = 0.85$ and $R' = 0.53$ (WSW cluster, Fig. 7c); $\theta_1 = 32°$, $\theta_2 = 35°$, $\phi = 0.93$ and $R' = 0.67$ (NE cluster, Fig. 8a); $\theta_1 = 30°$, $\theta_2 = 44°$, $\phi = 0.69$ and $R' =$

0.52 (SE cluster, Fig. 8c) This implies that under low fluid pressure condition ($P_f < \sigma_2$) only limited range of fracture orientations are susceptible to reactivate. In each case, for determining the absolute P_f magnitude, pole to vein data are plotted in 3D Mohr circles. Recent studies by Mondal and Acharyya (2018), documented the depth of faulting and fracturing in close vicinity of the study area (Chitradurga granite) to be ~2.4km. Similar depth of fracturing has also been reported by Acharyya and Mondal (2019), from the elliptical clasts of conglomerate bed within the Chitradurga schist belt. We have considered this depth for determining the magnitude of the maximum compressive stress (σ_1) during fracture formation, using $\sigma_1 = h\rho g$, where h = depth of fracturing in metabasalts (~2.4km), ρ= approximate bulk density of crust (2700 kg/m3), g = 9.8 m/sec2. Therefore, $\sigma_1 \geq 63.5$ MPa, when depth of fracturing in metabasalt~2.4km. The studies by Ishii (2015) have shown that the laboratory-measured tensile strength is almost similar to the tensile crack initiation stress (σ_3). Eidelman and Reches (1992) have also shown that the minimum principal stress required for the generation of fractures in stiff inclusions (such as pebbles) may be considered to be identical to the laboratory measured tensile strength of the rock. Therefore, we have considered that the minimum principal stress (σ_3) required for fracture initiation in the metabasalt of the study area are equivalent to its tensile strength. Thus, the tensile strength of metabasalt (~12 MPa; obtained from BTS studies) indicates that the minimum compressive stress (σ_3) has to be $\sigma_3 \geq 12$ MPa. It is obvious that the magnitude of σ_3 could be greater than the one which is considered, but as we are dealing with the limiting condition, this is the minimum magnitude of σ_3 required to overcome the tensile strength of the rock and generate a fracture in the rocks.

It may also be noted that, previous studies by Mondal and Acharyya, 2018, conducted in Chitradurga Granite (to understand the fracturing in microgranioid enclaves), in close vicinity of the study area also

regarded the magnitude of σ_3 ~10 MPa, to be a good estimation. Combining these estimations with the results obtained from the present studies, we constrained the value for σ_3 ~12MPa.

310 In each case we consider the limiting values for both maximum and minimum compressive stresses. Magnitude for the intermediate compressive stress (σ_2) is determined using the respective stress ratios (ϕ) for both high and low P_f respectively. Following Jolly and Sanderson (1997), the 3D Mohr circles are constructed using the above magnitudes of principal stresses and the angles determining the range of fracture orientations. Thus, well-defined P_f lines for both high P_f (P_f=53.2 MPa; Fig. 7b) and low P_f

315 conditions (P_f=39.3 MPa; Fig. 7d, P_f=46.5, Fig. 8b and P_f=38.8, Fig. 8d) are obtained using the Fractend code (Github, 2017).

4.4 Dilation tendency, slip tendency and fracture susceptibility

Dilation tendency (T_d) and slip tendency (T_s) determine the propensity of any fracture orientation to

320 reactivate through dilation or shearing, under a certain state of stress condition (Mazzarini et al., 2019). While, high dilation tendency ensures reactivation through dilation, high slip tendency elevates chances of opening through shearing (Ferrill et al., 1999). According to, Stephens et al., 2017, fracture planes suffer dilation when the difference between σ_1 and the normal stress acting on the plane is close enough to the magnitude of differential stress($\sigma_D = \sigma_1 - \sigma_3$) and $T_d = (\sigma_1 - \sigma_n)/ \sigma_D$. Slip

325 tendency is denoted by the ratio of shear stress (σ_s) to normal stress (σ_n); ($T_s = \sigma_s/\sigma_n$) and also depends on the frictional characteristics of the rock (Morris et al., 1996), along with the fracture plane orientation. Under a particular state of stress condition if the ratio of shear stress to normal stress is significantly large, then that particular fracture orientation is susceptible to reactivate. Fracture susceptibility (S_f), is defined

as the variation of fluid pressure (ΔP_f) within a fracture plane that can lead to fluid induced shear

330 reactivation (Mildren et al., 2002; Stephen et al., 2017). Such reactivations depend on the shear and

normal stresses acting on the fracture plane, along with the cohesion (= 0 in this case) and the static

coefficient of friction (μ_s); $S_f = \sigma_n - (\sigma_s/\mu_s)$.

Lower hemisphere equal area projections (see Fig. 9) of the poles to fracture (vein-filled) data help us to

understand the variation in dilation tendency, slip tendency and susceptibility of fractures with respect to

335 their orientations, under both high and low P_f conditions. The diagrams are prepared using Fractend code

(Github, 2017). It is evident from figure 9a, that the dilation tendency is high for the fracture orientations

which are at a high angle to the σ_3 axis, i.e., pole to these fractures form a well-defined cluster around σ_3.

These fractures show greater tendency towards dilational opening for both high and low P_f (Fig. 9a and

b). For fracture orientations having higher slip tendency, i.e., susceptible to shear opening, pole to the

340 fractures are at a low angle to the σ_3 axis. The fracture planes are therefore oriented at an angle to the

maximum compressive stress axis σ_1, condition favorable for shear reactivation for both, high and low P_f

(Fig. 9c and d). Fracture susceptibility, which involves variation in fluid pressure (ΔP_f) is low for the

fracture orientations having high dilation and slip tendencies, which indicates fluid-induced fracture

reactivation in metabasalts (Fig. 9e and f) in the study area.

345

4.5 Paleostress analysis

The shallow to moderaly plunging normal faults of the study area with prominent slip directions are used

to determine the stress regime under which these fractures and faults were formed and reactivated. Fault-

slip data (orientations of fault planes and slip directions) recorded from the field were used for paleostress

350   determination. Several methods are proposed for paleostress analyses using fault-slip data (e.g. Angelier,

1994; Dupin et al., 1993; Etchecopar et al., 1981; Gapais et al., 2000; Marrett and Allmendinger, 1990;

Ramsay and Lisle, 2000; Twiss and Unruh, 1998; Yamaji, 2000; Žalohar and Vrabec, 2007 and the

references therein). Since, the fault-slip analysis methods are well established, here we prefer to represent

only the salient aspects. The fault-slip analysis can be divided into two categories based on whether the

355   fault-slip data are viewed as representing kinematic or dynamic information (Blenkinsop 2006; Gapais et

al. 2000; Twiss & Unruh,1998) based on the following assumptions: (1) bulk state of stress is uniform

and movement on the fault planes are independent of each other; (2) slip on the fault plane occurs along

the direction of the maximum resolved shear stress under a given stress state (Wallace–Bott Hypothesis);

(3) faults are homogeneous and a part of the same tectonic event (Angelier, 1994; Gapais et al., 2000;

360   Gephart & Forsyth, 1984; Twiss & Unruh, 1998). In this study, we have determined the paleostress

direction, using fault-slip data measured from 73 shallow to moderately dipping normal faults (spatially

distributed) in the metabasalt by Right Dihedron method. Since, some of the fault planes show variation

in their strike orientations, the small amount of inhomogeneity in the data set is reduced in this process.

Thus, the data sets are segregated methodically into homogeneous data subsets using the 'Win_Tensor'

365   software program (version 5.8.6; Delvaux and Sperner, 2003; Delvaux, 2011). In the present analysis all

the collected data are represented in a single set and separation is done by using the Right Dihedron

method without any sort of manual intervention. Following Delvaux and Sperner, 2003, the data is filtered

on the basis of stress ratio (R), orientation of the stress axes and symmetry of the measured sets. Out of

73 data, 30 data are accepted with a low value of counting deviation and nominal counting values of 0

370   and 100 for σ_1 and σ_3 respectively. Thus, the best fitted reduced stress tensor is obtained for the accepted

data subset (30 out of 73 fault data; see Fig. 10) at a "C" quality ranking. It also provides the relative orientations of the principal stress axes, stress ratio (R= 0.72) and stress regime index (R´=1.25). The NNE-SSW directed extension direction obtained from this paleostress analysis (see Fig. 10) coincides well with the regional D3 extension direction. Data rejected in this process to obtain the best fit stress tensor when treated separately yields, NNE-SSW oriented extension direction with small variations in the R and R´ values. According to Delvaux and Sperner (2003), the obtained stress regime index indicates a pure-strike slip domain which is in a good agreement with sinistral shearing along CSZ.

5 Discussions

5.1 Fabric development vs. regional tectonics

It has been mentioned earlier that the metabasalts of the study area lack any distinct visible foliation. However, the AMS analysis suggests, a prominent NNW-SSE to NW-SE oriented magnetic fabric in metabasalts. This magnetic fabric also matches well with the field foliation of the meta-sedimentary sequences, surrounding the metabasalts and is also parallel to the regional trend of CSZ (see Fig. 2). This implies that the fabric in metabasalts of the study area must have been controlled by the regional D1/D2 deformation under ~NE-SW directed shortening that generated the field foliation in the meta-sedimentary sequences. Recently Mondal and Mamtani (2014) and Mondal (2018) interpreted that, the ~NW-SE oriented magnetic fabric in the adjacent younger granites of the study area are the result of co-axial (pure shear) deformation. Since these fabric in metabasalts and adjacent younger granites are found to be parallel and manifested by the same NE-SW shortening, it is inferred that magnetic fabric in the metabasalts of the study area are also the result of co-axial deformation. The magnetic lineations in the

metabasalts, plunge due NNW through sub-vertical to SSE (Fig. 5b). In the previous studies, these variations in the plunge of the magnetic lineations had been interpreted as a consequence of superposed deformation (e.g., Mamtani and Sengupta, 2010; Mondal and Mamtani, 2013). Field investigations also reveal the presence of dome basin structure in the metasedimentary rocks of the region (Mondal and Mamtani, 2013; Chakrabarti et al., 2006). Therefore, in the light of regional structural information and above discussions, it is inferred that these variations in magnetic lineations of the metabasalts are the manifestation of dome-basin geometry that were produced due to the superposition of D3 over D1/D2 regional deformation. Recently, Mondal (2018) documented similar results from the vorticity analysis from the magnetic fabric data in adjacent Chitraurga granite. The studies by Bhatt et al., (2017); Mondal and Acharyya (2018), suggest that the D1/D2 deformation lasted between 2614 and 2555 Ma while the D3 deformation is approximated around ~2537 Ma."

5.2 Control of regional far-field stress on developing the brittle structures in Chitradurga region.

The above discussions suggest that (a) NNW-SSE oriented magnetic foliation developed during D1/D2 deformation under NE-SW directed shortening, (b) variation in plunge of magnetic lineation is a manifestation of dome-basin geometry on account of D3 deformation. It is argued that during D3 deformation under NW-SE to E-W directed shortening the CSZ evolved as a sinistral shear zone (Mondal and Acharyya, 2018). It may be noted that the angle between the mean orientation of the schist belt and the compression direction for D3 deformation are found to be ~45º which also supports the sinistral movement along Chitradurga shear boundary.

It is mentioned in sections 2 and 3 that, the study area is replete with a number of brittle structures such as fractures and faults. At places, these fractures are filled-up with quartz veins. Therefore, it is now essential to evaluate whether and how these brittle structures and their kinematics can be fitted to the regional far-field stresses responsible for deformation in the Chitradurga region. The quartz vein orientation data from northern part of the Chitradurga schist belt reveals that the vein emplacement took place during regional D3 deformation (Mondal and Mamtani, 2014). Recently, Mondal and Acharyya (2018), and Acharyya and Mondal (2019) suggested that the brittle structures (fractures/faults) in the Chitradurga granite (in close vicinity to the study area) are related to the D3 deformation. Moreover, paleostress investigation using fault-slip data also reveals NNE-SSW directed extension was dominant during D3 deformation. Apart from this, evidences of any later deformation, i.e., post D3 deformation, have not been recorded from the study area (from previous studies and as per our field observations). Thus, based on the present studies and above discussions, it is logically inferred that the formation of brittle structures (fractures/faults) as well as vein emplacement must be explained as a consequence of regional D3 deformation at a shallow depth. Mondal and Mamtani (2014) suggested that the Mulgund granite (2555 ± 6 Ma; Sarma et al., 2011), which lies in close vicinity to the metabasalts of the Chitradurga region, was emplaced syn-tectonically with CSZ. It is shown that the Mulgund granite underwent ductile deformation as it cooled and crystallized syn-tectonically with D3 deformation. The ductile deformation features in the granite were then superimposed by brittle structures during late D3, when the granite was fully solidified and had achieved a shallow depth (Mondal and Mamtani, 2016).Since both the lithologies (metabasalts and granite) have undergone same deformation and the fractures in them developed syntectonically with adjacent CSZ, it is favourable to interpret that the brittle structures, such as fractures

and faults in metabasalts developed on account of late D3 deformation under NW-SE to E-W directed compression at a shallow depth of about ~ 2.4 Km. For evaluating the nature (mode) of fracturing in the metabasalts of the study area, we used tensile strength (T) to be12 MPa (from BTS studies). We estimated $\Delta\sigma$= 51.5 MPa, which is greater than 4T, suggesting that the fractures in the metabasalts are not purely tensile, except for the cracks parallel to D3 shortening direction. However, the calculated value of $\Delta\sigma$ is less than 5.7T, indicating that the normal stress on the fractures are not purely compressive also. Therefore, the value of $\Delta\sigma$ satisfies 4T <$\sigma_1 - \sigma_3$< 5.7 T (Sibson, 2000), indicating that these fractures in the study area are extensional shear mode fractures.

5.3 Regional tectonics and the mechanism of fracturing, faulting

We discussed earlier in sect. -3, that the fractures and faults recorded in the metabasalts show a wide range of orientations with NNW-SSE maxima and WNW-ESE to NE-SW sub-maxima respectively (Fig. 4b). Among which, fractures trending along WNW-ESE to E-W are sub-parallel to the D3 (late phase) shortening direction. As previously mentioned in sect. -3, these WNW-ESE trending fractures have been regarded as tensional fractures. Similar orientations have also been recorded and interpreted as tensile fractures from the micro-granitoid enclaves in Chitradurga granite as evident from the studies of Mondal and Acharyya (2018). However, it is essential to explain the predominance of fractures and faults along the NNW-SSE orientation (forming the maxima). In order to explain this, we refer to the pre-existing fabric in the metabasalts of the study area, i.e., the NNW-SSE to NW-SE oriented magnetic fabric developed during D1/D2 regional deformation (Fig. 5a). Earlier studies suggest, that fractures are more likely to propagate along a pre-existing anisotropy, if and when the anisotropy is favorably oriented with

respect to the regional stress field (Ikari et al., 2015). The CSZ being a sinistral shear zone exhibits a pure

455   strike slip stress regime, coeval with D3 deformation (NW-SE to E-W directed shortening).

In the later phase of D3 deformation, the favorably oriented NNW-SSE fabrics were reactivated under a compatible stress field, thereby, causing reactivation of the pre-existing fabrics in the metabasalts. This however, fails to justify the occurrence of the ~NW-SE and ~NE-SW oriented fractures within the metabasalts. From field investigations, the NE-SW oriented fractures show dextral movements, while the

460   NNW-SSE and NW-SE oriented fractures are recorded with sinistral movements respectively (see Fig. 3c and d). However, the fracture disposition and consistency in their respective orientations indicate that all of these fractures are coeval, related to the same deformational event and have been reactivated under similar stress conditions. Moreover, any other brittle deformational event post D3, have not been recorded from the study area as mentioned earlier. Therefore, we need to explain the occurrence of such variably

465   oriented fractures/faults within a single kinematic framework. The NNW-SSE and NW-SE orientations are most likely to be sinistral, whereas NE-SW orientations form the dextral shear components respectively, considering CSZ to be the sinistral shear boundary. (See Fig. 11b and 4b, c). Thus, the NNW-SSE to NW-SE (P, Y and R) and the NE-SW to ENE-WSW (X and R′) fractures coincide with the shear components of a riedel shear system considering the angle of internal friction (Φ) in metabaslts of

470   the study area to be ~30˚. It may be noted that the value of Φ is approximated from the Uniaxial Compressive Strength (UCS) studies of the metabasalts core samples following Sivakugan et al., 2014.

These fracture planes (P, Y, R, X and R′) acted as pathways for fluid flow and vein emplacement during the late D3 deformation.

5.4 Understanding the mechanism of fluid flow and vein emplacement in Chitradurga region

In order to explain the vein emplacement mechanism along these weak zones we need to consider the fluid pressure conditions that prevailed at the time of vein emplacement. In sect. 4.4, we mentioned earlier that the lower hemisphere equal area projection of pole to vein data shows girdle distribution, indicating high P_f condition (~53.2 MPa; >σ_2) in the study area. Under such high P_f conditions, veins were emplaced along all possible orientations, including NNW-SSE, NW-SE, WNW-ESE, NE-SW and ENE-WSW trending fractures. The building fluid pressure surpassed the normal stresses acting on the fracture wall, and hence, fluid burped into the weak planes leading to fluid-induced reactivation of the fractures, promoting vein emplacement along them (Fig. 11c). However, the NNW-SSE trending veins show greater thickness and abundance with respect to other orientations (see Fig. 4d and 3e). We found that pole to these veins (NNW-SSE trending orientations) lie within the warm zones of the stereoplots obtained from the Fractend code (Github, 2017), indicating higher dilation tendencies (see Fig. 9a and 9b). In Fig. 9a and 9b, it is perceived that pole to these orientations form a cluster around the σ_3 stress axis. Similarly, pole to the orientations trending NW-SE and NE-SW respectively, have higher slip tendencies, indicating shear reactivation along them (Fig. 9c and d). Most of the poles to the NNW-SSE trending orientations lie within the overlapping warm zones, indicating high potential to reactivate in both shear and dilation mode (high slip and dilation tendencies). These orientations are susceptible for dilation as well as shear reactivation, depending on the predominance of fluid pressure and availability of fluid for inducing

dilation or shear reactivation. Availability of fluid significantly reduces the effective normal stress (σ_n' $=\sigma_n$- P_f); where σ_n' and σ_n are the effective normal stress and normal stress respectively) acting on the fracture planes (see Fig. 11c and d). Under this condition, fluid burps into the fractures leading to a significant drop in the fluid pressure. This sudden drop in the fluid pressure reduces the solubility of fluid materials promoting deposition of vein followed by sealing of the pathways (Cox et al., 1991, 2001). Pathways thus remains sealed till the next cycle of fluid pressure build up, fracture reactivation and vein deposition. However, in between two such cycles of high fluid pressure, intermediate low fluid pressure cycles persist, during which fluid pressure might not be substantially high to reactivate all the pre-existing pathways. Thus, a high fluid pressure cycle is followed by subsequent pulses of low fluid pressure causing selective reactivation of some of the pre-existing orientations. The orientations represented by the individual clusters (WSW, NE and SE) can be reactivated selectively depending on their respective orientation to the tectonic stress field and the fluid pressure magnitude. Hence, it is envisaged that, these cycles of high and low P_f conditions might have been repeated multiple times (n-times) until the fluid source was completely exhausted. In the present case, the low P_f conditions are interpreted by discretely analyzing the clusters within the girdle distribution of pole to vein data in the lower hemisphere equal area projection. (see sect. 4.4). Such low P_f could not surpass the normal stresses of all the pre-existing pathways. And only the NNW-SSE oriented ones (related to the magnetic fabric of the metabasalts) having high dilation and slip tendencies were favorably oriented for reactivation and fluid flow. The above mechanism of *fault-valve action* is supported with field evidences showing occurrences of thick quartz veins enclosing angular chunks of metabasalt hosts with multiple sub-parallel fault planes (identified from the slickenside lineations), see Fig. 3e & 3f. Quartz veins with multiple median lines indicate

predominance of crack-seal mechanism due to cyclic fluid ingression (Fig. 3g). This suggests that the

515 process of fracturing, fracture reactivation through faulting and vein emplacement (*fault-valve* action)

prevailed throughout the D3 deformation. Thus, the process of new fracture formation and reactivation

were continuously persistent during the entire late D3 phase, with intermittent episodes of vein

emplacement under both high and low P_f conditions.

520 **7 Conclusions**

In the present study, we commented on the vein emplacement mechanism of the Chitradurga greenstone

belt (Dharwar craton, south India). We analysed the magnetic fabric data recorded from AMS analysis of

the metabasalt that hosts the quartz veins. 3D Mohr circle and paleostress analysis have been used to

evaluate the vein emplacement vs. regional deformation. Following are the main findings and conclusions

525 from the study:

1. The NW-SE oriented magnetic fabric recorded in the metabasalts (as evident from the AMS
   analysis) is a product of the D1/D2 regional deformation on account of NE-SW directed
   shortening. This fabric was also favourably oriented and therefore, suitable for fracture
   propagation in relation to the prevailing stress field.

530 2. D3 deformation manifested by NW-SE to E-W directed shortening was coeval with the sinistral
   movement along CSZ. It is concluded that during late D3 deformation all pre-existing fabrics and
   the ones constituting the riedel shear system were reactivated, with CSZ acting as a shear
   boundary.

3. The variably oriented fractures and faults i.e., the NNW-SSE, NW-SE, WNW-ESE, NE-SW and ENE-WSW oriented ones are identified as the P, Y, R, T, X and R´ shear components of the riedel shear system. The NNW-SSE oriented shears (P, Y and R) are abundant owing to their favourable correspondence with the pre-existing AMS fabric.

4. Paleostress analysis using fault-slip data recorded from field studies reveals NNE-SSW directed extension, asserting reactivation under a WNW-ESE directed compression (related to D3 deformation).

5. Vein emplacement took place under both high and low P_f conditions. It is envisaged that multiple number of such alternating high and low P_f cycles prevailed in the process of fluid flow and vein emplacement in the region.

6. Vein emplacement took place along all possible orientations. Evidences of *fault-valve behaviour* and fluid induced fracture/fault reactivation have been recorded from field studies. However, the NNW-SSE trending orientations having higher values of slip and dilation tendencies, channelized fluid during both high and low P_f conditions, thereby attaining maximum vein thickness.

7. The process of fracture formation, reactivation and faulting prevailed under a far field compression related to late D3 deformation. However, intermittent episodes of fluid pressure build up led to fluid induced faulting, rupturing and vein emplacement in the region.

Author contribution: SB: conceptualization, methodology, data curation, formal analysis, writing. TKM: supervision, conceptualization, methodology, data curation, funding acquisition, writing.

555 **Competing interests:** The authors declare that they have no conflict of interest.

Acknowledgments

The study is funded by DST-SERB (File No. ECR/2015/000079) and RUSA 2.0 to TKM. This study is a part of SB's doctoral research; being funded by DST Inspire (IF170912). Geological Survey of India 560 (Bangalore) is acknowledged for helping with logistic support and discussions during fieldwork. Prof. Manish A. Mamtani is thanked for allowing the authors to use KLY-4S Kappabridge system (IIT Kharagpur, India) for AMS analysis. Prof. Arindam Basu and Dr. Bikash K. Ram are thanked for helping with tensile strength measurements using GCTS$^{©}$ at IIT Kharagpur, India. Detailed reviews by Prof. Francesco Mazzarini and Prof. C. Pascal helped to improve the paper considerably. Editorial handling by 565 Prof. Roger Soliva is gratefully acknowledged. Assistance provided by Ayan Patsa, Subha Saha and Swarnasree Mondal are acknowledged. SB also acknowledges the wholehearted support of Sunil Kumar Bhowmick and Gouri Bhowmick.

References

Acharyya, S.S., Mondal, T.K.: Stress enhanced tensile fractures in elliptical clast in conglomerate. Journal of Structural Geology 122 (2019) 81–88, https://doi.org/10.1016/j.jsg.2019.02.001, 2019.

Angelier, J., 1994.: Fault slip analysis and palaeostress construction. In: Hancock, P.L. (Ed.), Continental Deformation. Pergamon Press, London.

ASTM (2001) American Society for Testing and Materials. ASTM Standards on Disc, 04.08. West Conshohocken, PA, 2001.

Attewell, P.B., Sandford, M.R.: Intrinsic shear strength of a brittle, anisotropic
Rock-I. Experimental and mechanical interpretation. Int. J. Rock Mech. Min.
Sci. Geomech. Abstract. 11, 423-430, 1974.

Aydin A, Basu A.: The use of Brazilian test as a quantitative measure of rock weathering. Rock Mech Rock Eng 39:77–85, https://doi.org/10.1007/s00603-005-0069-0, 2006.

Baer, G., Beyth, M., Reches, Z.: Dikes emplaced into fractured basement, Timna Igneous Complex, Israel. Journal of Geophysical Research 99, 24039–24051, https://doi.org/10.1029/94JB02161, 1994.

Basu, A., Mishra, D.A., Roychowdhury, K.: Rock failure modes under uniaxial compression, Brazilian, and point load tests. Bull EngGeol Environ (2013) 72:457–475, http://dx.doi.org/10.1007%2Fs10064-013-0505-4, 2013.

Beckinsale, R. D., Drury, S. A., Holt, R. W.: 3305–Myr old gneisses from south
Indian craton. Nature 283, 469–470, 1980.

Bhatt, S., Rana, V., Mamtani, M.A.: Deciphering relative timing of fabric development in granitoids withsimilar absolute ages based on AMS study (Dharwar Craton, South India). Journal of Structural Geology 94 (2017) 32-46, https://ui.adsabs.harvard.edu/link_gateway/2017JSG....94...32B/doi:10.1016/j.jsg.2016.11.002, 2017.

Blenkinsop, G. T.: Kinematic and dynamic fault slip analyses: implications from the surface rupture of the 1999 Chi–Chi, Taiwan, earthquake, Journal of Structural geology, 28, 1040–1050, https://doi.org/10.1016/j.jsg.2006.03.011, 2006.

Boullier, A. M., Robert, F.: Palaeoseismic events recorded in Archaean gold quartz vein networks, Val d'Or, Abitibi, Quebec, Canada. Journal of Structural Geology14, 161–179, https://doi.org/10.1016/0191-8141(92)90054-Z, 1992.

Chadwick, B., Vasudev, V. N., Hedge, G. V.: The Chitradurga schist belt and its adjacent plutonic rocks NW of Tungabhadra, Karnataka: a duplex in the late Archean convergent setting of the Dharwar craton. Journal of the Geological Society of India 61, 611–613, 2003.

Chadwick, B., Ramakrishnan, M., Vasudev, V. N., Viswanatha, M. N.: Facies Distributions and Structure of a Dharwar Volcano sedimentary Basin: Evidence for Late Archaean transpression in Southern India? Journal of the Geological Society of London 146, 825–834, 1989.

Chakrabarti, C., Mallick, B. S., Pyne, T. K., Guha, D.: A manual of the Geology of India. Geological Survey of India, Kolkata, 2006.

Chardon, D., Peucat, J.–J., Jayananda, M., Choukroune, P., Fanning, C.M.: Archaean granite–greenstone tectonics at Kolar (south India): interplay of diapirism and bulk inhomogeneous contraction during juvenile magmatic accretion. Tectonics 21, 1–17, https://doi.org/10.1029/2001TC901032, 2002.

Cox, S. F., Knackstedt, M. A., Braun, J.: Principles of structural control on permeability and fluid flow in hydrothermal systems. Society of Economic Geologists Reviews 14, 1–24, 2001.

Cox, S. F.: Faulting processes at high fluid pressures: an example of fault–valve behaviour from the Wattle Gully Fault, Victoria, Australia. Journal of Geophysical Research 100, 12841–12860, https://doi.org/10.1029/95JB00915, 1995.

Cox, S. F., Wall, V. J., Etheridge, M. A., Potter, T. F.: Deformational and metamorphic processes in the formation of mesothermal vein–hosted gold deposits — examples from the Lachlan Fold Belt in central Victoria, Australia. Ore Geology Reviews 6, 391–423, https://doi.org/10.1016/0169-1368(91)90038-9, 1991.

620 Cucci, L., Luccio, F.D., Esposito, A., Ventura, G.: Vein networks in hydrothermal systems provide constraints for the monitoring of active volcanoes. Scientific reports 7:146, https://dx.doi.org/10.1038%2Fs41598-017-00230-8, 2017.

Delaney, P. T., Pollard, D. D., Zioney, J. I., McKee, E. H.: Field relations between dikes and joints: emplacement processes and palaeostress analysis. Journal of Geophysical Research 91 (B5),
625 4920–4938, doi.org/10.1029/JB091iB05p04920, 1986.

Delvaux, D.: EGU General Assembly. Win-tensor, an Interactive Computer Program for Fracture Analysis and Crustal Stress Reconstruction, vol. 13 , Geophysical Research Abstract, Vienna, 2011

Delvaux, D., Sperner, B.: Stress tensor inversion from fault kinematic indicators and focal mechanism
630 data: the TENSOR program. In: Nieuwland, D. (Ed.), New Insights into Structural Interpretation and Modelling: Geol. Soc. Lond. Special Publication 212, 75–100, 2003.

Donath, F.A.: Experimental study of shear failure in anisotropic rocks. Geol. Soc. Am. Bull. 72, 985-990, 1961.

Dupin, J. M., Sassi, W., Angelier, J.: Homogeneous stress hypothesis and actual fault slip: a distinct
635 element analysis. Journal of Structural Geology 15, 1033–1043, doi.org/10.1016/0191-8141(93)90175-A, 1993.

Eidelman, A., Reches, Z.: Fractured pebbles—A new stress indicator. Geology 20 (4), 307-310, https://doi.org/10.1130/0091-7613(1992)020%3C0307:FPANSI%3E2.3.CO;2, 1992.

Etchecopar, A., Vasseus, G., Daigniers, M.: An inverse problem in microtectonics for the determination
640 of stress tensor from fault striation analysis, Journal of Structural Geology 3, 51–65, DOI: 10.1016/0191-8141(81)90056-0, 1981.

Ferrill, D.A., Winterle, J., Wittmeyer, G., Sims, D., Colton, S., Armstrong, A., Morris, A.P., 1999. Stressed rock strains groundwater at Yucca Mountain, Nevada. GSA Today 9, 1–8.

Gapais, D., Cobbold, P. R., Bourgeois, O., Rouby, D., de Urreiztieta, M.: Tectonic

645   Significance of fault–slip data, Journal of structural Geology. 22, 881–888, doi.org/10.1016/S0191-8141(00)00015-8, 2000.

Gephart, J. W., Forsyth, D. W.: An improved method for determining the regional stress tensor using earthquake focal mechanism data: application to the San Fernando earthquake sequence, Journal Geophysical Research 89(B11), 9305–9320, **doi.org/10.1029/JB089iB11p09305**, 1984.

650 GitHub, 2017. FracTend MATLAB code. https://github.com/DaveHealy-Aberdeen/FracTend

Gopalakrishna, G., Shareef, M., Nagesh, P.C., 2018. Shear-Controlled Gold Mineralization of G. R.Halli Area of Chitradurga Schist Belt, DharwarCraton: Insights from Fluid Inclusion Study. Open Journal of Geology, 8, 662-673, DOI: 10.4236/ojg.2018.87039 , 2018.

Gudmundsson, A., 2011. Rock Fractures in Geological Processes. Cambridge UniversityPress.

655 Gupta, S., Jayananda, M., Fareeduddin, 2014. Tourmaline from the Archean G.R. Halli Gold Deposit, Chitradurga Greenstone Belt, Dharwar Craton (India): Implications for the Gold Metallogeny. Geoscience Frontiers, 5, 877-892, doi.org/10.1016/j.gsf.2013.12.004, 2014.

Hoek, E.: Fracture of anisotropic rock. J. South Afr. Inst. Min. Metal. 64 (10), 501-518, 1964.

660 Hrouda, F., Chlupáčová, M., Pokorný, J.: Low–field variation of magnetic susceptibility measured by the KLY–4S Kappabridge and KLF–4A magnetic susceptibility meter: Accuracy and interpretational programme. Studia Geophysica et Geodaetica 50, 283–299, 2006.

Ikari, M.J., Neimeijer, A.R., Marone, C.: Experimental investigation of incipient shear failure in foliated rock. Journal of Structural Geology 77, 82-91, doi.org/10.1016/j.jsg.2015.05.012, 2015.

665 Ishii, E.: Far-field stress dependency of the failure mode of damage-zone fractures in fault zones: Results from laboratory tests and field observations of siliceous mudstone. Journal of Geophysical Research: Solid Earth, 70-91, tp://dx.doi.org/10.1002/2015JB012238, 2015.

ISRM, Suggested methods for determining tensile strength of rock materials. Int. J. Rock Mech. Min. Sci. & Geomech. Abstr., Vol. 15, 99-103, 1978.

670 Jayananda, M., Chardon, D., Peucat, J.–J., Capdevila, R.: 2.61 Ga potassic granites and crustal reworking in the western Dharwar craton, southern India: tectonic, geochronologic and geochemical constraints. Precambrian Research 150, 1–26, DOI: 10.1016/j.precamres.2006.05.004, 2006.

Jelínek, V.: Characterization of magnetic fabric of rocks. Tectonophysics 79, T63–T67, DOI:10.1016/0040-1951(81)90110-4, 1981.

675 Jolly, R.J.H., Sanderson, D.J. : A Mohr circle reconstruction for the opening of a pre-existing fracture. Journal of Structural Geology 19, 887-892, DOI. 10.1016/S0191-8141(97)00014-X, 1997

Lahiri, S., Mamtani, M.A.: Scaling the 3-D Mohr circle and quantification of paleostress during fluid pressure fluctuation–Application to understand gold mineralization in quartz veins of Gadag (southern India). Journal of Structural geology 88, 63–72, doi.org/10.1016/j.jsg.2016.05.003, 2016.

680 Logan, J. M., Dengo, C. A., Higgs, N. G., Wang, Z. Z.: Fabrics of experimental fault zones: their development and relationship to mechanical behaviour. In: Evans, B. & Wong, T. (eds) Fault Mechanics and Transport Properties of Rocks. Academic Press, San Diego, CA, 33–67, 1992.

Loock, S., Diot, H., Van Wyk de Vries, B., Launeau, P., Merle, O., Vadeboin, F., Petronis, M.S.: Lava flow internal structure found from AMS and textural data: An example in methodology from the
685 Chaîne des Puys, France. Journal of Volcanology and Geothermal Research 177, 1092–1104, doi.org/10.1016/j.jvolgeores.2008.08.017, 2008.

Maffione, M., Hernandez-Moreno, C., Ghiglione, M.C., Speranza, F., van Hinsbergen, D.J.J., Lodolo, E.: Deformation of the Southern Andes since the Late Cretaceous: constraints from anisotropy of magnetic susceptibility (AMS). Tectonophysics 665, 236–250,
690 doi.org/10.1016/j.tecto.2015.10.008, 2015.

Mamtani, M.A., Greiling, R.O.: Granite emplacement and its relation with regional deformation in the Aravalli Mountain Belt–inferences from magnetic fabric. Journal of Structural Geology 27, 2008–2029, doi.org/10.1016/j.jsg.2005.06.004, 2005.

Mamtani, M.A., Sengupta, P.: Significance of AMS analysis in evaluating superposed folds in quartzites.
695 Geological Magazine 147, 910–918, DOI: 10.1017/S0016756810000397, 2010

Marchesini, B., Garofalo, P.S, Menegon, L., Mattila, J., Viola, G.: Fluid-mediated, brittle–ductile deformation at seismogenic depth –Part 1: Fluid record and deformation history of fault veins in a nuclear waste repository (Olkiluoto Island, Finland). Solid Earth, 10, 809–838, doi.org/10.5194/se-10-809-2019, 2019.

700 Marrett, R., Allmendinger, R. W.: Kinematic analysis of fault–slip data , J.Struc.Geol. 12, 973–986. doi.org/10.1016/0191-8141(90)90093-E, 1990.

Martínez-Poza, A. I., Druguet, E., Castaño, L. M., Carreras, J.: Dyke intrusion into a pre-existing joint network: The Aiguablava lamprophyre dyke swarm (Catalan Coastal Ranges). Tectonophysics 630, 75–90, doi.org/10.1016/j.tecto.2014.05.015, 2014.

705 Mazzarini, F., Isola, I.: Hydraulic connection and fluid overpressure in upper crustal rocks: evidence from geometry and spatial distribution of veins at Botrona quarry, southern Tuscany, Italy. Journal of Structural Geology 29, 1386-1399, doi.org/10.1016/j.jsg.2007.02.016, 2007.

Mazzarini, F., Musumeci, G., Viola, G., Garofalo, P.S., Mattila, J.: Structural and lithological control on fluid circulation, dilation and ore mineralization (Rio Albano mine, Island of Elba, Italy). Journal
710 of Structural Geology 126 (2019) 210–230, doi.org/10.1016/j.jsg.2019.06.012, 2019.

McKeagney, C.J., Boulter, C.A., Jolly, R.J.H., Foster, R.P.: 3-D Mohr Circle analysis of vein opening, Indarama lode-gold deposit, Zimbabwe: implications for exploration. Journal of Structural Geology 26, 1275-1291, doi.org/10.1016/j.jsg.2003.11.001, 2004.

Mondal, T.K., Acharyya, S.S.: Fractured micro-granitoid enclaves: a stress marker. Journal of Structural
715 Geology 113, 33–41, DOI: 10.1016/j.jsg.2018.05.011, 2018.

Mondal, T.K.: Evolution of fabric in Chitradurga granite (south India)-A study based on microstructure, anisotropy of magnetic susceptibility (AMS) and vorticity analysis. Tectonophysics 723, 149–161, doi.org/10.1016/j.tecto.2017.12.013, 2018.

Mondal, T.K., Mamtani, M.A.: Palaeostress analysis of normal faults in granite implications for
720 interpreting Riedel shearing related to regional deformation. Journal of Geological Society 173, 216–227, doi.org/10.1144/jgs2014-136, 2016.

Mondal, T.K., Mamtani, M.A.: Fabric analysis in rocks of the Gadag region (southern India)-implications for time relationship between regional deformation and gold mineralization. Tectonophysics 629, 238–249, DOI: 10.1016/j.tecto.2013.09.021, 2014.

725 Mondal, T.K., Mamtani, M.A.: 3-D Mohr circle construction using vein orientation data from Gadag (southern India) e implications to recognize fluid pressure fluctuation. J. Struct. Geol. 56, 45-56, doi.org/10.1016/j.jsg.2013.08.005, 2013.

Mildren, S.D., Hillis, R.R., Kaldi, J.: Calibrating predictions of fault seal reactivation in the Timor Sea. APPEA J.42 (1), 187–202, 2002

730 Morris, A., Ferrill, D.A., Henderson, D.B., 1996. Slip-tendency analysis and fault reactivation. Geology 24, 275–278.

Naqvi, S.M., Rogers, J.J.W.: Precambrian geology of India: Oxford monographs on geology and geophysics No. 6. Oxford University Press, New York. 1987

Petit, J. P., Wibberley, C. A. J., Ruiz, G.: `Crack±seal', slip: a new fault valve mechanism? Journal of
735 Structural Geology 21, 1199-1207, 1999, 10.1016/S0191-8141(99)00038-3.

Ramakrishnan, M., Vaidyanadhan, R., 2010. Geology of India. Vol. 1. Geological Society of India, Bangalore.

Ramadass, G., Himabindu, D., Srinivasulu, N., 2003. Structural appraisal of the Gadag schist belt from gravity investigations. Proceedings of the Indian Academy of Sciences (Earth and Planetary
740 Science) 112, 577–586.

Ramsay, J.G. & Lisle, R.J.: The Techniques of Modern Structural Geology. Vol. 3: Applications of Continuum Mechanics in Structural Geology. Academic Press, London, 2000.

Raposo, M.I.B., D'Agrella–Filho, M.S., Pinese, J.P.P.: Magnetic fabrics and rock magnetism of Archaean and Proterozoic dike swarms in the southern São Francisco Craton, Brazil. Tectonophysics 443,
745 53–71 doi.org/10.1016/j.tecto.2007.08.001, 2007.

Sanderson, D. J., Zhang, X., 1999. Critical stress localization of flow associated with deformation of well–fractured rock masses, with implications for mineral deposits. In: McCaffrey, K. J. W.,

Lonergan, L. and Wilkinson, J. J. (Eds.) Fractures, Fluid Flow and Mineralization. Geological Society of London, Special Publications 155, 69–81.

750   Sarma, D. S., Fletcher, I. R., Rasmussen, B., McNaughton, N. J., Mohan, M. R., Groves, D. I.: Archean gold mineralization synchronous with late cratonization of the Western Dharwar Craton, India: 2.52 Ga U–Pb ages of hydrothermal monazite and xenotime in gold deposits. Mineralium Deposita 46, 273–288, DOI: 10.1007/s00126-010-0326-3, 2011.

Sibson, R. H.: A brittle failure mode plot defining conditions for high flux–flow. Economic Geology 95,
755   41–48, 10.2113/gsecongeo.95.1.41, 2000.

Sibson, R. H., Robert, F., Poulsen, K. H.: High–angle reverse faults, fluid–pressure cycling, and mesothermal gold–quartz deposits. Geology 16, 551–555, doi.org/10.1130/0091-7613(1988)016<0551:HARFFP>2.3.CO;2, 1988

Sibson, R. H., Scott, J.: Stress/fault controls on the containment and release of over pressured fluids:
760   examples from gold–quartz vein systems in Juneau, Alaska,Victoria, Australia, and Otago, New Zealand. Ore Geology Reviews 13, 293–306, 10.1016/S0169-1368(97)00023-1, 1998.

Sibson, R. H.: Structural permeability of fluid–driven fault–fracture meshes. Journal of Structural Geology 18, 1031–1043, doi.org/10.1016/0191-8141(96)00032-6, 1996.

Sibson, R. H.: Implications of fault–valve behaviour for rupture nucleation and recurrence.
765   Tectonophysics 211, 283–293, doi.org/10.1016/0040-1951(92)90065-E, 1992.

Sivakugan, N., Das, B. M., Lovisa, J., Patra, C. R.: Determination of c and w of rocks from indirect tensile strength and uniaxial compression tests. International Journal of Geotechnical Engineering 8, 59-65, doi.org/10.1179/1938636213Z.00000000053, 2014.

Stephens, T.L., Walker, R.J., Healy, D., Bubeck, A., England, R.W., McCaffrey, K.J.: Igneous sills record
770   far-field and near-field stress interactions during volcano construction: Isle of Mull, Scotland. Earth Planet. Sci. Lett. 478, 159–174. doi.org/10.1016/j.epsl.2017.09.003, 2017.

Tarling, D. H., Hrouda, F., 1993. The Magnetic Anisotropy of Rocks. Chapman and Hall, London.

Taylor, P.N., Chadwick, B., Moorbath, S., Ramakrishnan, M., Viswanatha, M.N.: Petrography, chemistry and isotopic ages of Peninsular Gneiss, Dharwar acid volcanic rocks and the Chitradurga granite

775   with special reference to the late Archaean evolution of the Karnataka craton. Precambrian Research 23, 349- 375. 10.1016/0301-9268(84)90050-0, 1984.

Thyng, K.M., Greene, C.A., Hetland, R.D., Zimmerle, H.M., DiMarco, S.F,: True Colors of Oceanography Guidelines for Effective and Accurate Colormap Selection. Oceanography, 9-13, doi.org/10.5670/oceanog.2016.66, 2016

780 Tsidzi, K. E. N.: The influence of foliation on point load strength anisotropy of foliated rocks. Engineering Geology 29, 49–58. 10.1016/0013-7952(90)90081-B, 1990.

Twiss, R. J., Unruh, J. R.: Analysis of fault slip inversions; do they constrain stress or strain rate? , Journal of Geophysical Research 103 (B6), 12205–12222, **doi.org/10.1029/98JB00612**.1998.

Vishnu, C. S., Lahiri, S., Mamtani, M. A.: The relationship between magnetic anisotropy, rock-strength

785   anisotropy and vein emplacement in gold-bearing metabasalts of Gadag (South India). Tectonophysics 722, 286-298, doi.org/10.1016/j.tecto.2017.09.011. 2018.

Yamaji, A., Sato, K.: Clustering of fracture orientations using a mixed Bingham distribution and its application to paleostress analysis from dike or vein orientations. Journal of Structural Geology 33, 1148-1157. DOI: 10.1016/j.jsg.2011.05.006, 2011.

790 Yamaji, A., Sato, K., Tonai, S.: Stochastic modeling for the stress inversion of vein orientations: Paleostress analysis of Pliocene epithermal veins in south western Kyushu, Japan. Journal of Structural Geology 32, 1137–1146. DOI: 10.1016/j.jsg.2010.07.001, 2010.

Yamaji, A.: The multiple inverse methods: a new technique to separate stresses from heterogeneous fault-slip data, Journal of Structural Geology 22, 441–452. DOI: 10.1016/S0191-8141(99)00163-7

795   2000.

Žalohar, J., Vrabec, M.: Paleostress analysis of heterogeneous fault–slip data: the Gauss method, Journal of Structural Geology 29, 1798–1810. DOI: 10.1016/j.jsg.2007.06.009, 2007.

800
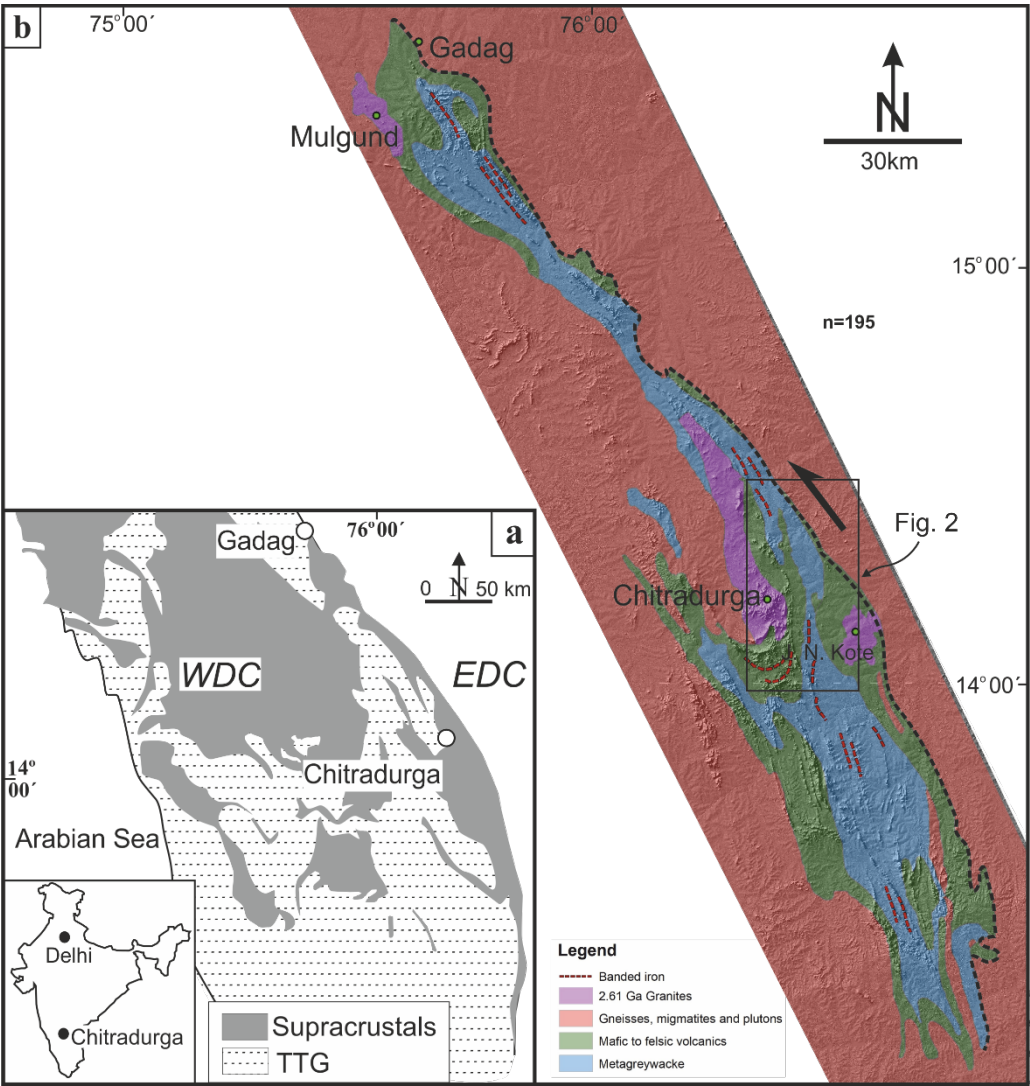
Figures:

Figure 01: (a) Regional map of western Dharwar craton, South Indian Shield [after Chadwick et al., 2003]. Inset shows the map of India. EDC = Eastern Dharwar Craton; WDC = Western Dharwar Craton, TTG=Tonalite-Trondhjemite-Granodiorite; Supracrustals=volcano-sedimentary assemblages. (b) Regional geological map (DEM) of the Chitradurga Schist Belt [modified after Jayananda et al., 2013]. Dotted line (in *b*) marks the eastern boundary of the Chitradurga Schist Belt, representing the Chitradurga Shear Zone (CSZ). Rectangular box near Chitradurga demarcates the study area.
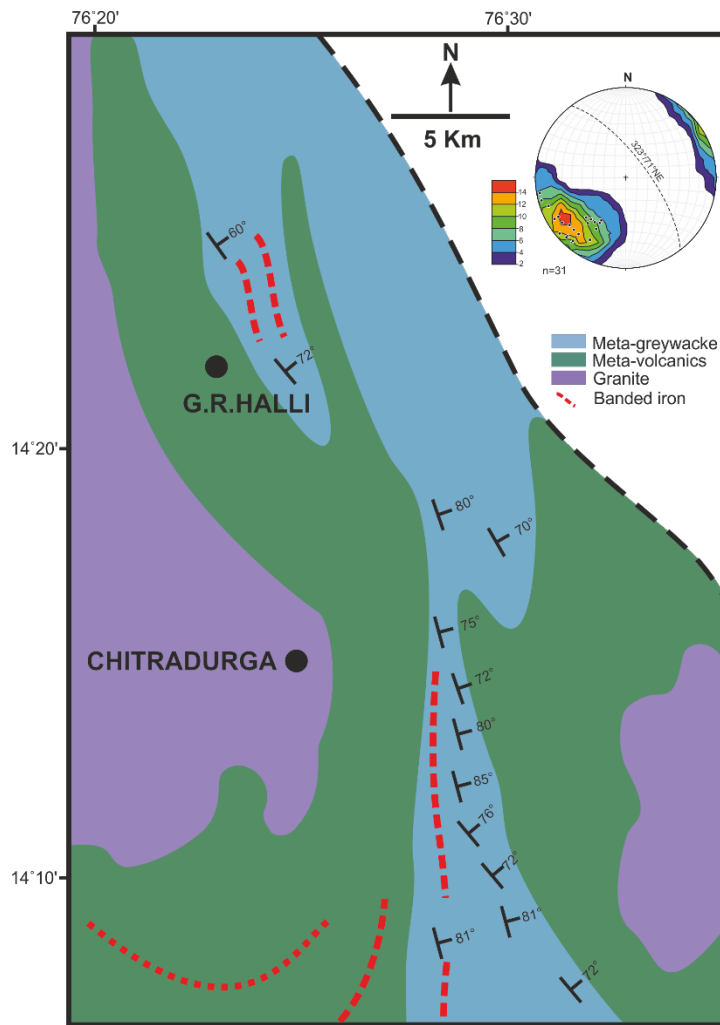
Figure 02: Geological map of the study area showing the foliation trends of the supracrustals. Lower hemisphere equal area projection shows the pole to foliation planes recorded from the region. Note that the mean foliation (dotted great circle) is 323º/71ºNE which is parallel to the CSZ (n= number data). Color scheme of the legend indicates variation in the contour density.

895 **Figure 03**. Field photographs from the study area. (a) Criss-cross orientation of quartz veins in metabasalt. (b) Close-up of a quartz vein in metabasalt showing crystal growth direction perpendicular to the vein wall. (c) Cross-cutting nature in quartz veins showing dextral displacement (marked by yellow half-arrows). (d) Wing cracks filled up with quartz veins associated with sinistral shearing (marked by yellow arrow).(e) NE dipping quartz vein showing slickenside lineations (maximum width recorded=120 cm),
900 inset showing close up of the fault plane found in e. Marker pen placed along the orientation of the slickenside lineations. (f) Angular chunks of metabasalt (enclaves) enclosed within faulted quartz vein. Dotted red line demarcates the enclave boundaries. Black arrow marks the slickenside lineation on the fault plane. (g) Field photograph of quartz vein (close view) showing multiple median lines (marked with red arrows) as an evidence of crack- seal mechanism. This clearly indicates cyclic fluid ingression and
905 fault valve action that led to the formation of veins in the metabasalts of the Chitradurga region. (h)Fault planes in metabasalt showing congruous steps (marked by yellow arrow). Blue arrow in the respective figures point towards N.

910

915
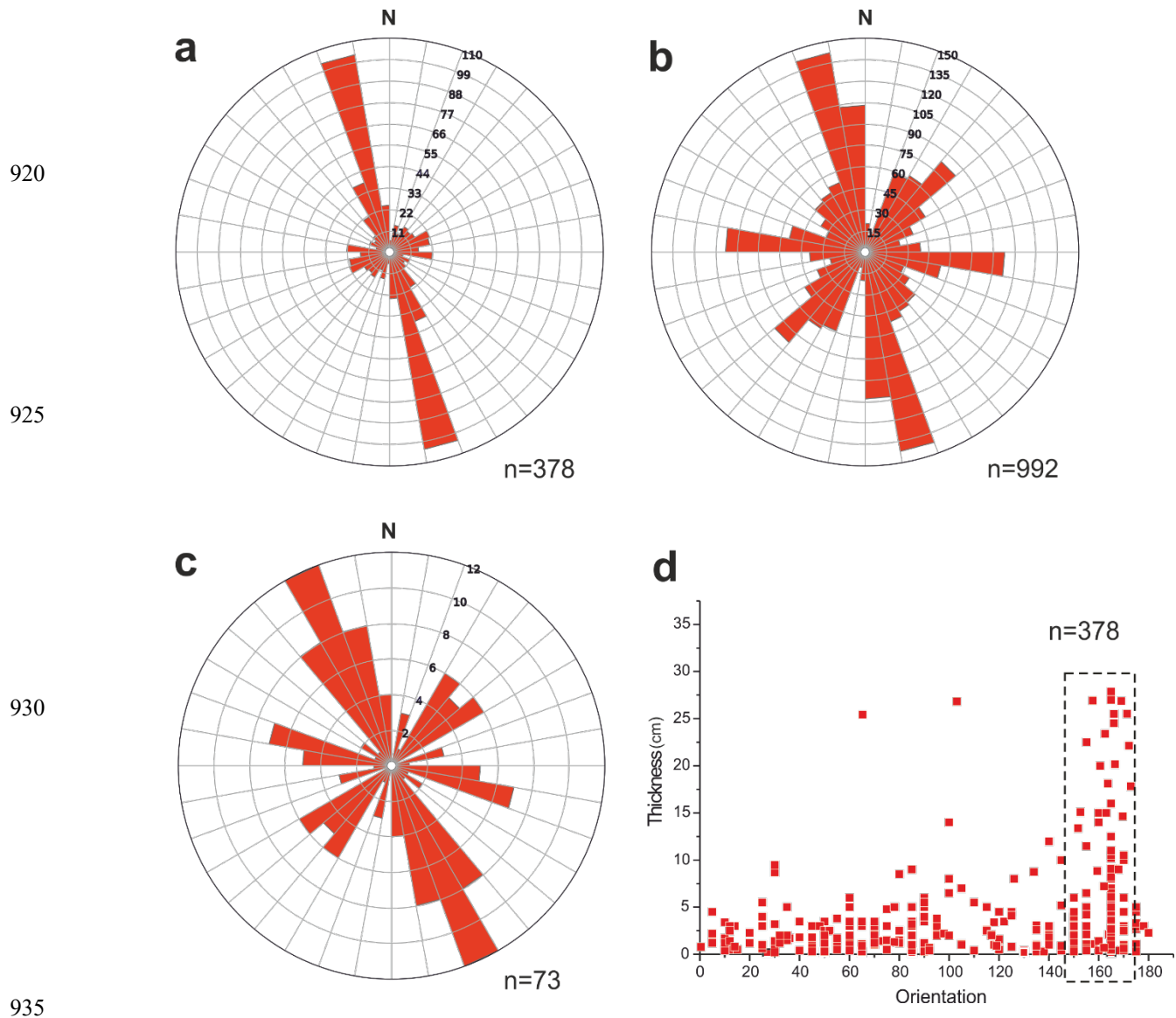
Figure 04. Rose diagrams and graphs of structural data recorded from the study area. (a), (b) and (c) are the rose diagrams of the strike orientation of the quartz veins, fractures and fault planes respectively. Note that the veins are mostly NNW-SSE striking whereas the fractures and fault planes show variable orientations, with a NNW-SSE maxima and a WNW-ESE to NE-SW sub maxima. (d) Graph of vein orientation vs. thickness, showing maximum vein thickness along NNW-SSE (marked with orange box). n= number of data.
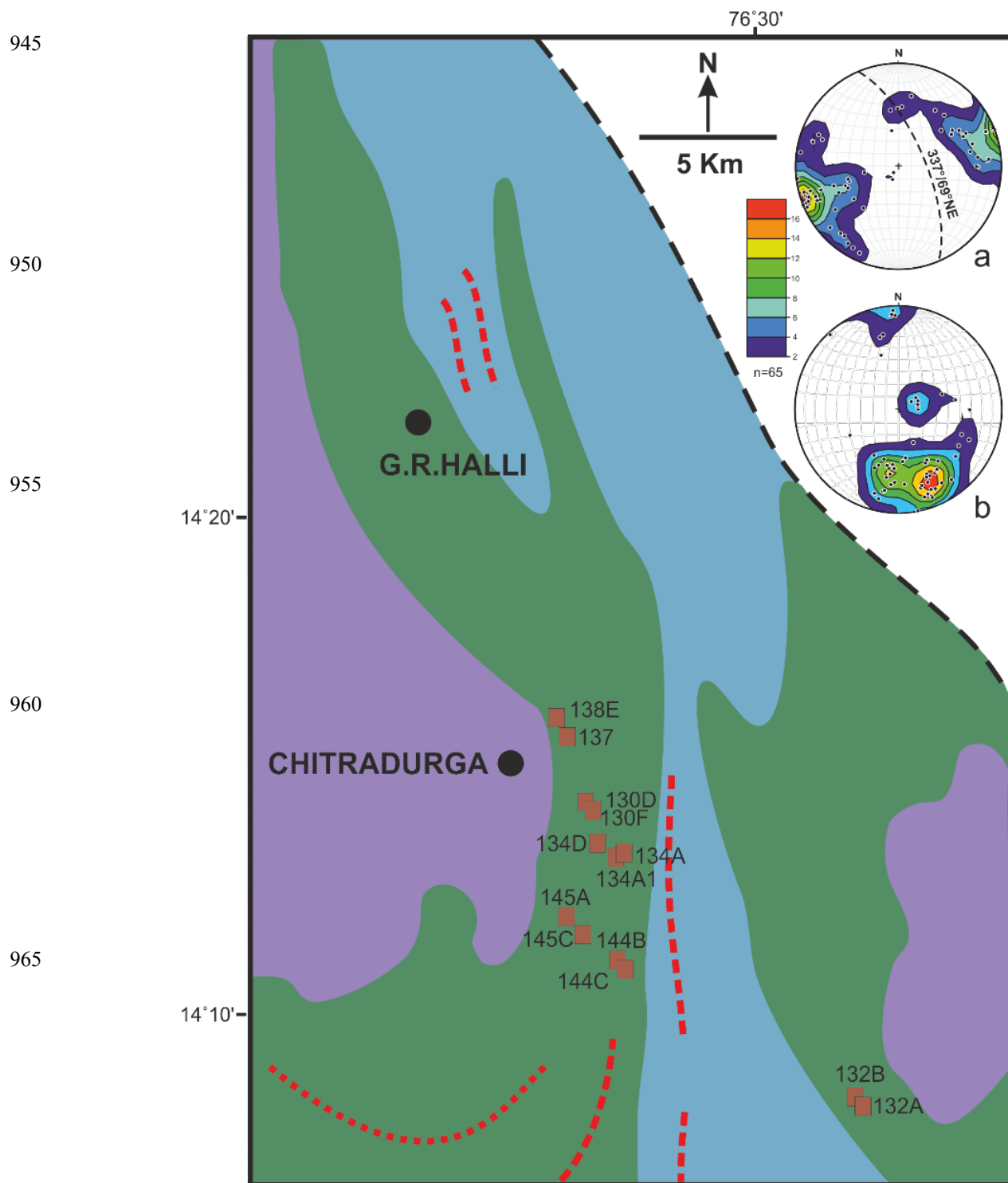
970

Figure 05. Map showing the location points (marked with brown boxes) from which oriented metabasalt samples for AMS analysis have been collected. (a) Lower hemisphere equal area projection of poles (K_3) to magnetic foliation (K_1K_2) plane. Mean orientation of K_1K_2 plane (dashed great circle)= 337º/69ºE (b) Lower hemisphere equal area projection showing the distribution of magnetic lineation (K_1).Color scheme of the legend indicates variation in the contour density.

980

Figure 06. Tensile strength determination of metabasalt samples. (a) Sample cores for Brazillian tensile strength (BTS) determination. Diameter: length=2:1. (b) Instruments used for measuring BTS. (c) Sample cores obtained after failure.

1000

1005
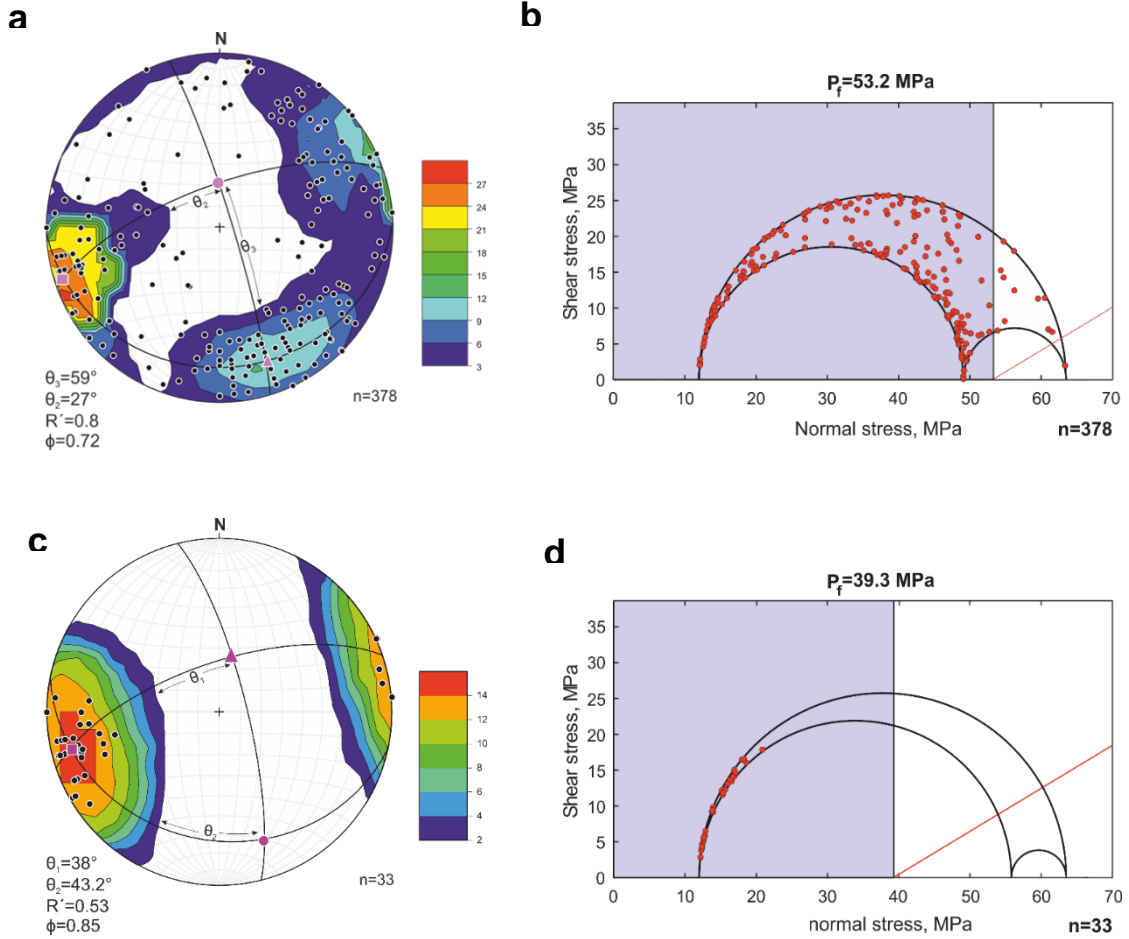
Figure 07. State of stresses and fluid pressure (P_f) conditions determined from vein orientation data in the study area. (a) Lower hemisphere equal area projection of pole to veins shows girdle distribution, implying $P_f > \sigma_2$ (following Jolly and Sanderson, 1997). The empty space devoid of any vein pole data helps to determine the position of σ_1 (using Bingham statistics of the Stereonet 9 software) and thereby defines $\sigma_1\sigma_2$ and $\sigma_1\sigma_3$ planes. Angles θ_2 and θ_3 are measured which are used to determine the stress ratio (ϕ) and driving pressure ratio (R′) respectively. Color scheme of the legends indicate variation in the contour density. Pink circle (σ_1), pink triangle (σ_2) and pink square (σ_3) respectively. (b) 3D Mohr circle diagram for high P_f conditions. Red line in the Mohr circle represents the reactivation envelope for cohesionless fractures. Vein pole data lying within the blue zone, i.e., to the left of the P_f (black) line represent fractures filled up with veins that are susceptible to reactivate (Fractend code available via

Github, 2017). (c) Lower hemisphere equal area projection of poles to vein data forming the SW cluster in (a), this cluster distribution of vein pole data indicates $P_f < \sigma_2$. Cluster maxima defines σ_3 axis. Angles θ_1 and θ_2 are measured and similarly ϕ and R´ are determined. (d) 3D Mohr circle diagram for low P_f condition. Only a limited range of fracture filled up with veins are susceptible to reactivate. Red dots represent pole to vein data, red line forms the reactivation envelope for cohesionless fractures.
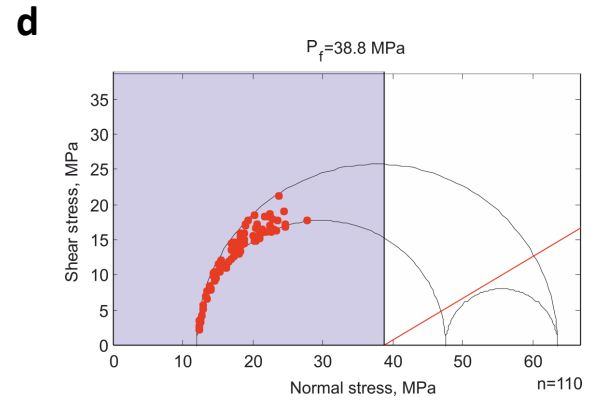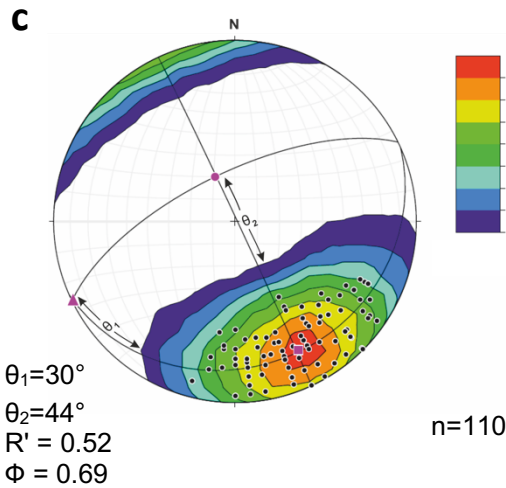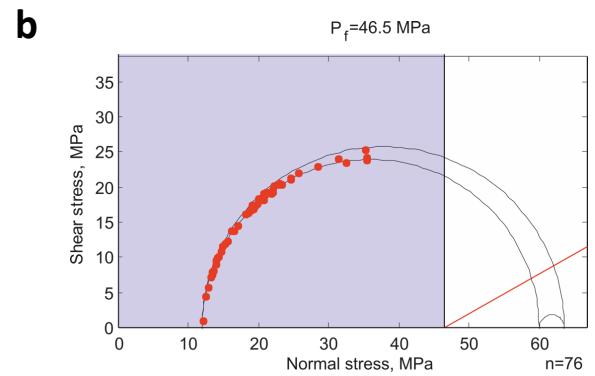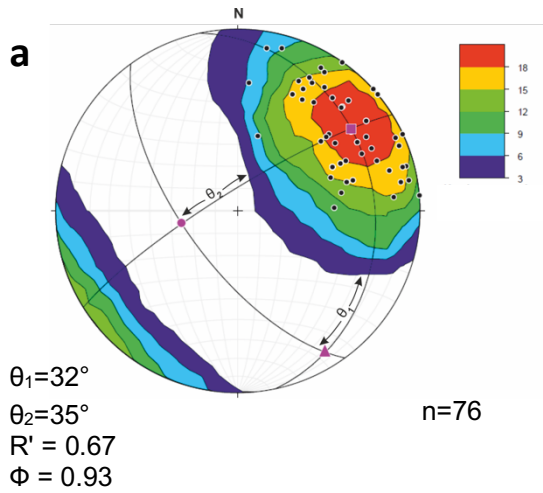
Figure 08. State of stress and fluid pressure (P_f) conditions determined from the vein orientation data in the study area. (a) Lower hemisphere equal area projection of poles to vein data forming the NE cluster. (b) 3D Mohr circle diagram for NE cluster. (c) Lower hemisphere equal area projection of poles to vein data forming the SE cluster. (d) 3D Mohr circle diagram for SE cluster. In the respective lower hemisphere equal area projections, cluster distribution of vein pole data indicates $P_f < \sigma_2$. Cluster maxima defines σ_3 axis. The ranges of fracture orientations (θ) are measured. Subsequently, ϕ and R' values are also determined similar to Fig 7. Pink circle (σ_1), pink triangle (σ_2) and pink square (σ_3) respectively. In the 3D Mohr circle diagrams, only a limited range of fracture filled up with veins are susceptible to reactivate. Red dots represent pole to vein data, red line forms the reactivation envelope for cohesionless fractures. Vein pole data lying within the blue zone, i.e., to the left of the P_f (black) line represent fractures filled up with veins that are susceptible to reactivate.
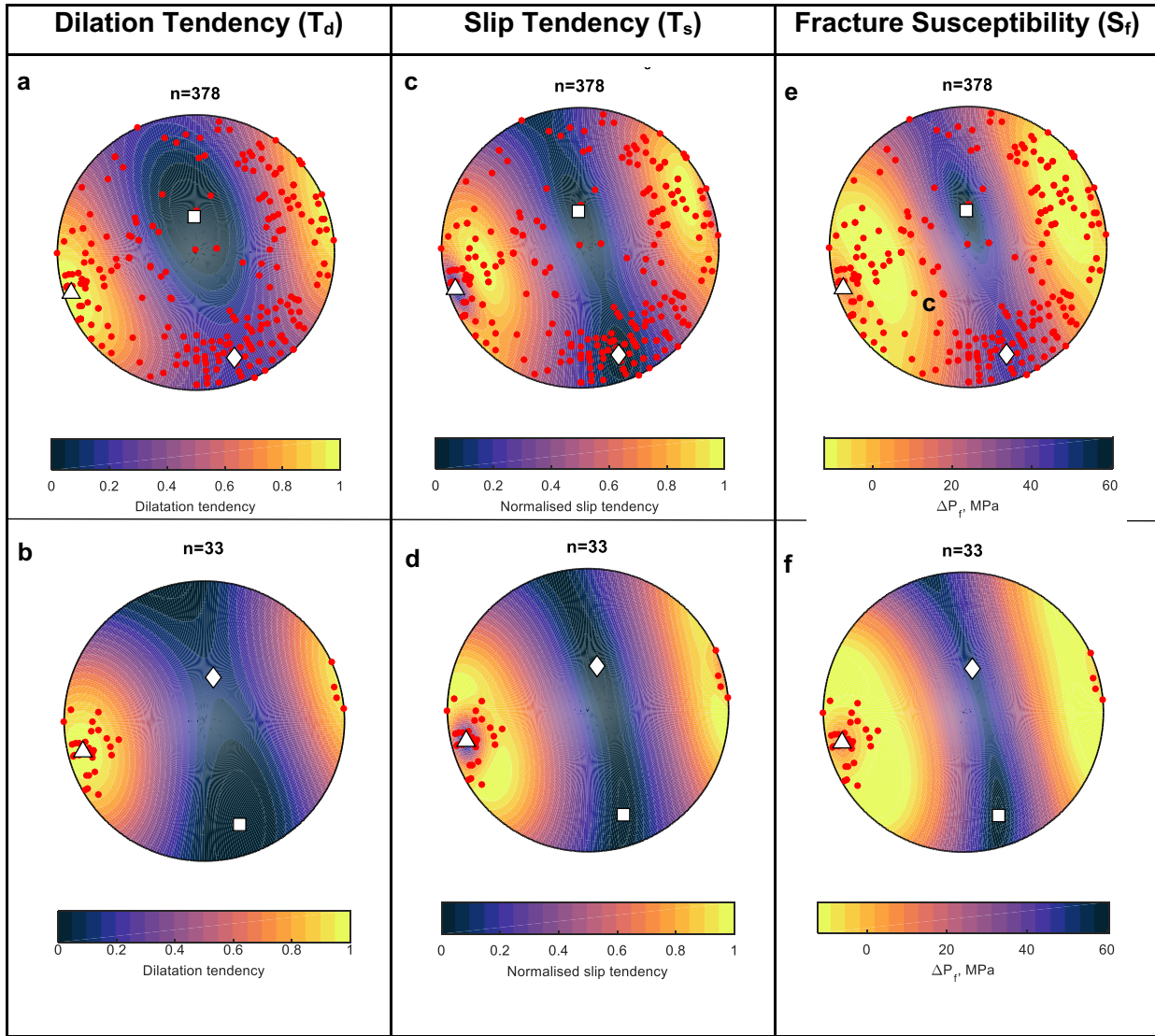
Figure 09. Lower hemisphere equal area projection for dilation tendency, slip tendency and fracture susceptibility in a given fluid pressure condition and for a specific stress state (Fractend code available via Github, 2017). (a) and (b) represents dilation tendency for high and low P_f. (c) and (d) represents slip tendency for high and low P_f. (e) and (f) fracture susceptibility for high and low P_f conditions respectively. Warm color zones in (a) and (b), represents vein orientations with higher propensity for tensional opening. In (c) and (d) warm colors indicate vein attitudes that suffered shearing. In (e) and (f) the warm color zones stand for vein attitudes that are more susceptible to reactivate under low P_f variation. 'Thermal' color scheme from Thyng et al., 2016. White square (σ_1), white diamond (σ_2) and white triangle (σ_3).
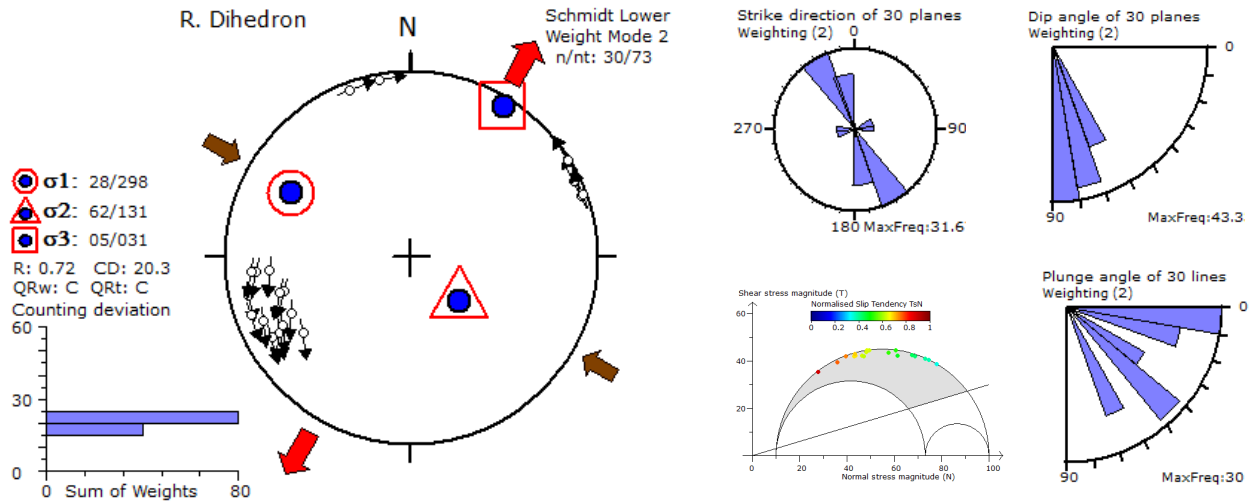
Figure 10. Paleostress analysis (using right dihedron method) of faults recorded in the metabasalts of the
study area; for both left lateral and right lateral normal faults. Red arrow marks the extension direction
(σ_3) and pink arrow marks the principal compression direction. The histogram shows the minimum values
for counting deviation. *n* and *nt* are the number of data accepted for tensor calculation and total number
of data respectively. R (stress ratio) = (σ_2-σ_3) / (σ_1-σ_3). Rose diagrams for fault plane strike, dip and plunge
variations are also presented in the top right corner. 3D Mohr diagrams demonstrate possible areas of
fault reactivation with variation in susceptibility, colored circles represent pole to the fault planes. The
failure envelope for Mohr's circle is based on Byerlee (1978) initial friction angle of 16.7^0. Note that the
maximum extension is along NNE-SSW direction.

a

N

Magnetic foliation

D1/D2 deformation

337°/69°NE

n=65

b

CSZ

D3 deformation

Magnetic foliation

R Y P **N**

X

R′

T

n=73

c

σ_3 σ_2

σ_1

High P$_f$ condition

σ_s

σ'_n

SiO$_2$ rich fluid influx under high P$_f$ condition

n times

d

σ_1

σ_3

σ_2

Low P$_f$ condition

σ_s

σ'_n

P$_f$

ΔP$_f$

Time

SiO$_2$ rich fluid influx under low P$_f$ condition
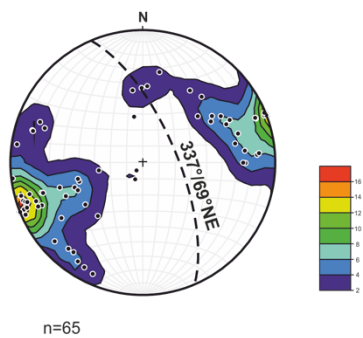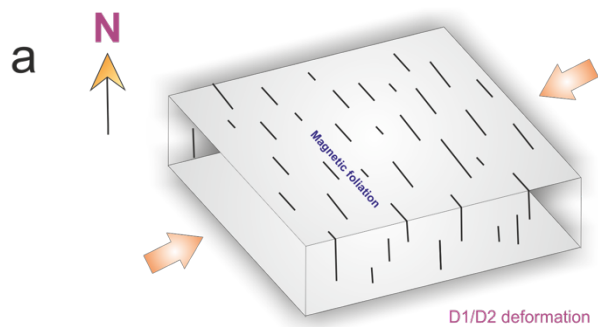
1160
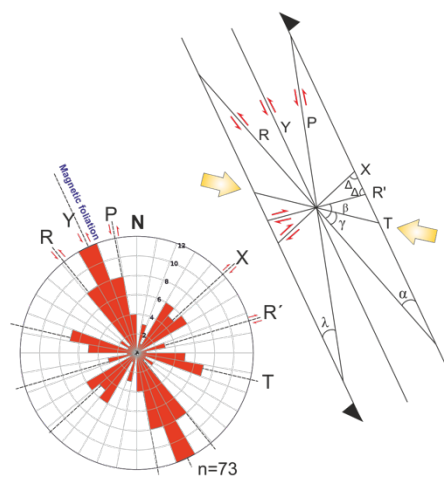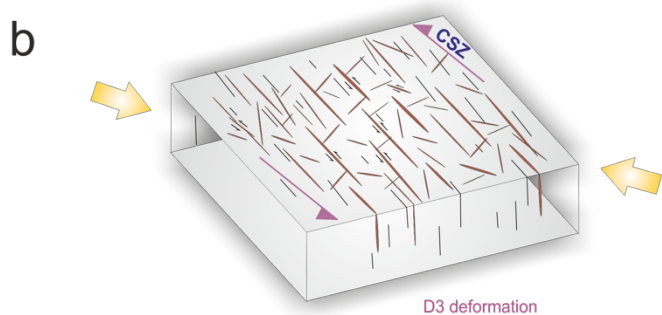
1165
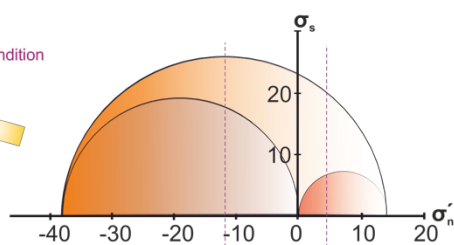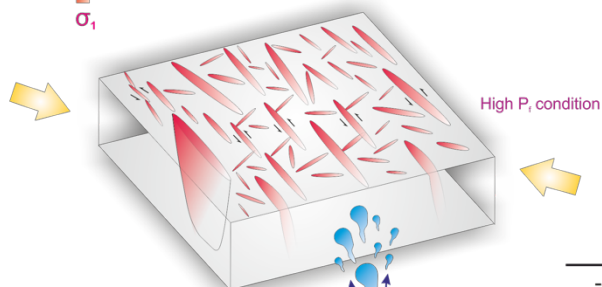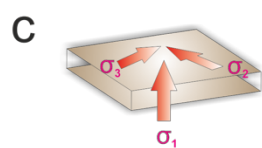
1170
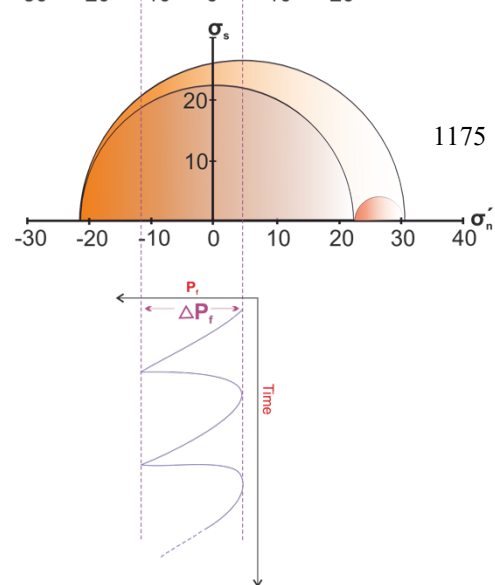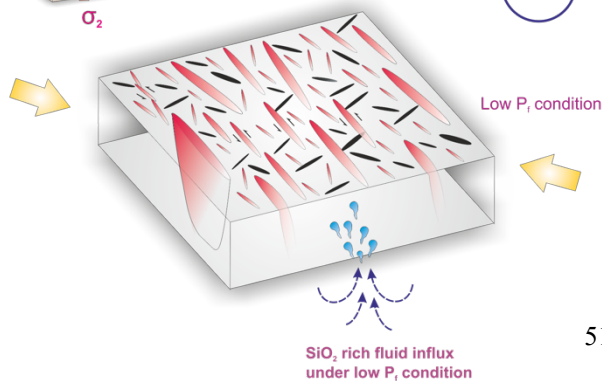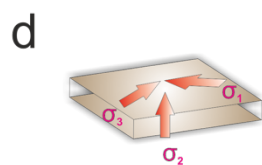
1175

Figure 11. Schematic model showing formation and reactivation of fractures, along with vein emplacement in the metabasalt host rock. (a) Development of the NNW-SSE to NW-SE oriented magnetic fabrics in the rock unit under a NE-SW shortening related to D1/D2 deformation. Lower hemisphere equal area projection shows mean orientation of the magnetic fabric $\sim$ 337º/69ºNE. (b) Formation of the Y, P, R, R´, X and T shears related to the riedel shear system under a NW-SE to E-W shortening related to the late D3 deformation (half arrows representing the shear zone boundary). The angles (α, β, γ, λ and Δ) between the shear components are given after Logan et al. 1992. $\Phi=30°$ (angle of internal friction) is measured from UCS studies of the samples from the study area. Corresponding riedel shear model, with CSZ as the shear boundary and rose diagram showing orientations of the respective shear components. (c) and (d) showing vein emplacement under high P_f and low P_f conditions respectively (state of stresses along the fracture planes are given, in c, σ_1 is vertical due to fluid overpressure). Corresponding 3D-mohr circle diagrams quantifying the effective normal stresses ($\sigma_n' = \sigma_n$- $P_{f;}$ in Mpa) under both high and low P_f conditions, difference in P_f ($\Delta P_f \sim$13.9 MPa), obtained from the dashed lines representing the mean stress in each case. A conceptual graph shows multiple cycles (n-times) of high and low P_f conditions in the study area justifying *fault-valve action* that led to the emplacement of vein in the Chitradurga region.